

Structure and dynamics of galaxies with a low surface-brightness disc - II. Stellar populations of bulges^{*}

L. Morelli^{1,2}, E. M. Corsini^{1,2}, A. Pizzella^{1,2}, E. Dalla Bontà^{1,2}, L. Coccato³,
J. Méndez-Abreu^{4,5} and M. Cesetti^{1,2}

¹ *Dipartimento di Fisica e Astronomia, Università di Padova, vicolo dell'Osservatorio 3, I-35122 Padova, Italy.*

² *INAF-Osservatorio Astronomico di Padova, vicolo dell'Osservatorio 5, I-35122 Padova, Italy.*

³ *European Southern Observatory, Karl-Schwarzschild-Straße 2, D-85748 Garching bei München, Germany.*

⁴ *Instituto Astrofísico de Canarias, C/ Vía Láctea s/n, E-38200 La Laguna, Spain*

⁵ *Departamento de Astrofísica, Universidad de La Laguna, C/ Astrofísico Francisco Sánchez, E-38205 La Laguna, Spain*

Draft version on 29 March 2021

ABSTRACT

The radial profiles of the H_{β} , Mg, and Fe line-strength indices are presented for a sample of eight spiral galaxies with a low surface-brightness stellar disc and a bulge. The correlations between the central values of the line-strength indices and velocity dispersion are consistent to those known for early-type galaxies and bulges of high surface-brightness galaxies. The age, metallicity, and α /Fe enhancement of the stellar populations in the bulge-dominated region are obtained using stellar population models with variable element abundance ratios. Almost all the sample bulges are characterized by a young stellar population, on-going star formation, and a solar α /Fe enhancement. Their metallicity spans from high to sub-solar values. No significant gradient in age and α /Fe enhancement is measured, whereas only in a few cases a negative metallicity gradient is found. These properties suggest that a pure dissipative collapse is not able to explain formation of all the sample bulges and that other phenomena, like mergers or acquisition events, need to be invoked. Such a picture is also supported by the lack of a correlation between the central value and gradient of the metallicity in bulges with very low metallicity. The stellar populations of the bulges hosted by low surface-brightness discs share many properties with those of high surface-brightness galaxies. Therefore, they are likely to have common formation scenarios and evolution histories. A strong interplay between bulges and discs is ruled out by the fact that in spite of being hosted by discs with extremely different properties, the bulges of low and high surface-brightness discs are remarkably similar.

Key words: galaxies : abundances – galaxies : bulges – galaxies : evolution – galaxies : stellar content – galaxies : formation – galaxies : Kinematics and Dynamics

1 INTRODUCTION

Galaxies with a central face-on surface brightness fainter than 22.6 mag arcsec⁻² in the B band are classified as low surface-brightness (LSB) systems. Although they are more difficult to be identified than high surface-brightness (HSB) galaxies, LSB galaxies do not occupy a niche in galactic astrophysics. Indeed, they constitute up to 50 per cent of the galaxy population and, consequently, represent one of the major baryonic repositories in the Universe (see Bothun et al. 1997, for a review). Most of LSB are dwarf galaxies with usually blue colour (Zackrisson et al. 2005; Vorobyov et al. 2009). Nevertheless, LSB galaxies are characterized by different morphologies (ranging from dwarf irregulars to giant spirals) and

cover a wide range of colors ($0.3 < B - V < 1.7$) suggesting that they can follow a variety of evolutionary paths. The typical gas surface density of LSB discs is below the critical threshold necessary for star formation, despite the fact that they have a higher content of neutral hydrogen with respect to their HSB counterparts (van der Hulst et al. 1993). This inability to condense atomic gas into molecular gas results in a very low star formation rate and in a significantly slower evolution of the galaxy.

Although most of the LSB galaxies are bulgeless, there are also galaxies with a LSB disc and a significant bulge component (Beijersbergen et al. 1999; Pizzella et al. 2008, hereafter Paper I). It is not known whether these bulges are similar to those of HSB galaxies and whether their properties do depend on the LSB nature of their host discs.

An invaluable piece of information to understand the processes of formation and evolution of bulges in LSB galaxies

^{*} Based on observations made with ESO Telescopes at the La Silla Paranal Observatory under programmes 76.B-0375 and 80.B-00754.

is imprinted in their stellar populations. To this aim, the central values and radial profiles of age, metallicity, and α/Fe enhancement of the stellar component can be used to test the predictions of theoretical models, as already done for the bulges of HSB galaxies (see Mehlert et al. 2003; Rampazzo et al. 2005; Sánchez-Blázquez et al. 2006; Annibali et al. 2007; Jablonka et al. 2007; Zhao 2012). Gas dissipation toward the galaxy centre with subsequent star formation and blowing of galactic winds produces a gradient in the radial profile of metallicity. Therefore, a metallicity gradient is expected in bulges formed via monolithic collapse (e.g., Kawata 2001; Kobayashi 2004). A relationship between the gradient steepening and galaxy mass is also expected (Pipino et al. 2010) as well as a strong gradient in α/Fe enhancement (Ferreiras & Silk 2002). However, according to Pipino et al. (2008) other processes have also to be taken into account to explain the observed abundance ratios. In particular, the interplay between the timescale of star formation and gas flows produces the metallicity gradient and in the meanwhile it flattens the gradient of α/Fe enhancement (Pipino et al. 2008). The metallicity gradient is expected to be very shallow (or even absent) in bulges built by merging (Bekki & Shioya 1999). In fact, dry mergers mix up the galaxy stars erasing the pre-existing population gradients (Pipino et al. 2010). The metallicity gradient is rarely enhanced by secondary events of star formation which eventually occur in wet mergers (Kobayashi 2004). If this happens, a clear signature has to be observed in the age radial profile for several Gyrs (Hopkins et al. 2009). The predictions for bulges assembled through long timescale processes, such as dissipationless secular evolution of the disc component, are more controversial. According to this scenario, the bulge formed by the redistribution of disc stars (Kormendy & Kennicutt 2004; Kormendy et al. 2009). The population gradients which are eventually present in the progenitor disc could be either amplified, since the resulting bulge has a smaller scale length than disc, or erased as a consequence of disc heating (Moorthy & Holtzman 2006).

Whereas the measurement of the emission lines in the optical spectra of LSB galaxies has been extensively performed to derive the metallicity of the ionized gas (Impey et al. 2001; Bergmann et al. 2003; Ramya et al. 2011; Liang et al. 2010), to date the properties of the underlying stellar populations have been obtained only in a few cases (Bergmann et al. 2003). To address this issue, here we present a detailed photometric and spectroscopic study of a sample of 8 bulges hosted in LSB discs. The analysis of the spectral absorption lines allowed us to derive the age and metallicity of the stellar populations and estimate the efficiency and timescale of the last episode of star formation in order to disentangle between early rapid assembly and late slow growing of the bulge.

The paper is organized as follows. The galaxy sample is presented in Section 2. The photometric and spectroscopic observations together with the data reduction and analysis are described in Section 3. The properties of the stellar populations of the bulges of the sample galaxies are investigated in Section 4. Finally, the conclusions are given in Section 5.

2 SAMPLE SELECTION

All the sample galaxies were selected to be spiral galaxies with a bulge and a LSB disc. Six of them were taken from Paper I and their broad-band images and long-slit spectra are already available to us. We therefore refer to Paper I for a detailed description of

the photometric and kinematic data we are using in this paper to measure the line-strength indices of these galaxies. In addition, two more late-type spirals were taken from the catalogue of candidate LSB galaxies by Impey et al. (1996). It should be noted that these galaxies have central surface brightnesses that place them on the low side of normal spirals, but are not examples of typical LSB galaxies. Nevertheless, the LSB nature of their discs was confirmed by a detailed decomposition of the surface-brightness distribution (see Section 3.3 for details). Therefore, the final sample is made by 8 LSB spiral galaxies with a morphological type ranging from Sa to Sm and including some barred galaxies. An overview of their basic properties which includes morphological type, size, apparent and absolute magnitude, and distance is given in Table 1 and their optical images are shown in 1.

3 OBSERVATIONS, DATA REDUCTION, AND ANALYSIS

3.1 Broad-band imaging and long-slit spectroscopy

The photometric and spectroscopic observations of PGC 26148 and PGC 37759 were carried out with the Very Large Telescope (VLT) of the European Southern Observatory (ESO) at Paranal Observatory on 2006 March 23-25 and 2008 February 17-18. The two galaxies were observed with the UT1 unit mounting the FOcal Reducer and low dispersion Spectrograph 2 (FOR2). The detector consists of a mosaic of 2 MIT/LL CCDID-20 CCDs separated by a gap of 480 μm along the spatial direction. Each CCD has 2048×4096 pixels of $15 \times 15 \mu\text{m}^2$. A 2×2 pixel binning was adopted giving a spatial scale of $0.25 \text{ arcsec pixel}^{-1}$ with a field of view of $6.8 \times 6.8 \text{ arcmin}^2$. The gain and readout noise were set to $1.43 e^- \text{ ADU}^{-1}$ and $2.90 e^-$ (rms), respectively.

For each galaxy three 20-s broad-band images were obtained with the R_special+76 filter centred at 6550 \AA with a FWHM of 1650 \AA .

The long-slit spectra were taken using the grism GRIS_1400V+18 with 1400 grooves mm^{-1} in combination with the $0.7 \text{ arcsec} \times 6.8 \text{ arcmin}$ slit. The wavelength range between 4560 and 5840 \AA was covered with a reciprocal dispersion of $0.64 \text{ \AA pixel}^{-1}$ after pixel binning. This set up guarantees an adequate oversampling of the instrumental broadening function. Indeed, the instrumental velocity resolution was 1.31 \AA (FWHM) corresponding to $\sigma_{\text{inst}} = 33 \text{ km s}^{-1}$ at 5000 \AA . It was estimated by measuring the width of the emission lines of a comparison arc spectrum after the wavelength calibration.

Major and minor-axis spectra were obtained for PGC 37759 ($P.A._{\text{MJ}} = 40^\circ$, $P.A._{\text{MN}} = 130^\circ$), whereas only major-axis spectra were taken for PGC 26148 ($P.A._{\text{MJ}} = 15^\circ$). For each position three 40-minutes spectra were taken. The position of the slit centre along the spatial direction was slightly drifted so that the gap between the two CCDs was imaged in different locations.

The standard calibration frames for imaging and spectroscopy (i.e., darks, biases, and flatfields) as well as the spectra of the comparison arc lamp were taken in the afternoon or at the twilight before each observing night. Spectrophotometric standards were observed to ensure the flux calibration of the spectra. The typical value of the seeing FWHM during the observing runs was 1.2 arcsec as measured by fitting a two-dimensional Gaussian to the field stars in the acquisition images.

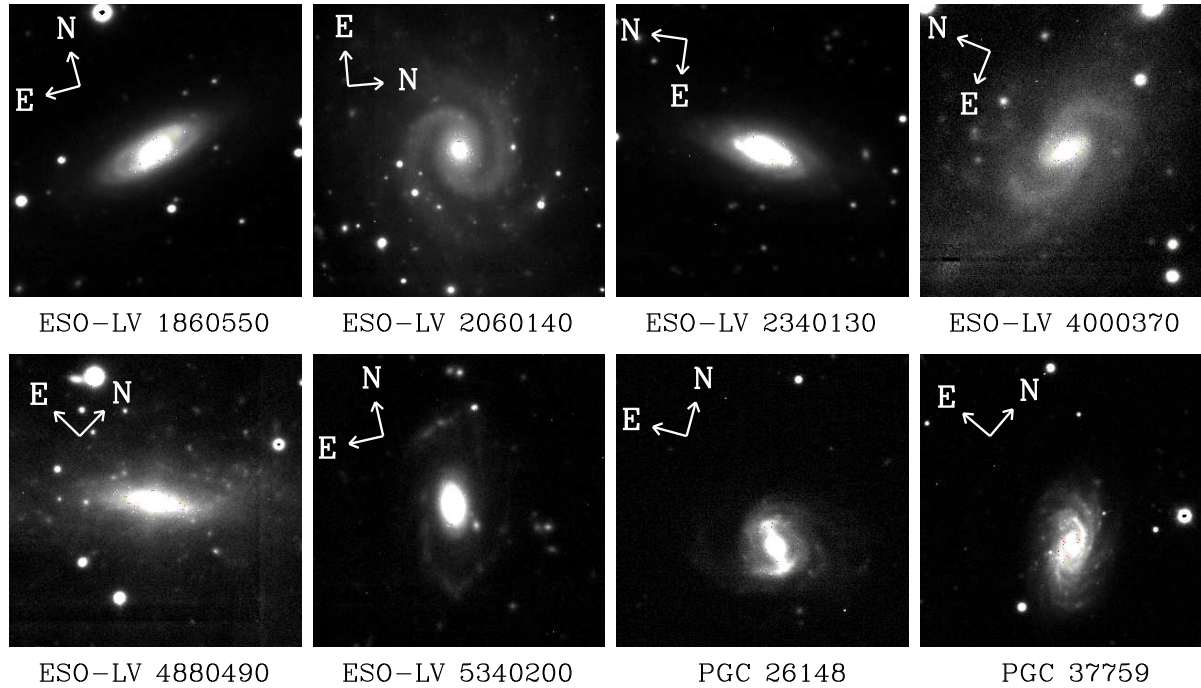


Figure 1. Optical images of the sample galaxies. The orientation is specified by the arrows indicating north and east in the upper-left corner of each image. The size of the plotted region is about $80 \text{ arcsec} \times 80 \text{ arcsec}$.

Table 1. Parameters of the sample galaxies. The columns show the following. Column (2): morphological classification from Lyon Extragalactic Database (LEDA); column (3): numerical morphological type from LEDA. The typical error on T is 1.0; column (4): apparent isophotal diameters measured at a surface-brightness level of $\mu_B = 25 \text{ mag arcsec}^{-2}$ from LEDA; column (5): total observed blue magnitude from LEDA; column (6): radial velocity with respect to the CMB reference frame from LEDA; column (7): distance obtained as V_{CMB}/H_0 with $H_0 = 75 \text{ km s}^{-1} \text{ Mpc}^{-1}$; column (8): absolute total blue magnitude from B_T corrected for extinction as in LEDA and adopting D ; column (9): source of the photometric and spectroscopic data: 1 = Paper I, 2 = this paper.

Galaxy	Type	T	$D_{25} \times d_{25}$ (arcmin)	B_T (mag)	V_{CMB} (km s^{-1})	D (Mpc)	M_{B_T} (mag)	Source
(1)	(2)	(3)	(4)	(5)	(6)	(7)	(8)	(9)
ESO-LV 1860550	Sab	2.0	1.7×0.6	13.96	4594	60.1	-19.93	1
ESO-LV 2060140	SABc	5.0	1.6×0.8	14.89	4672	60.5	-19.01	1
ESO-LV 2340130	Sbc	3.9	1.4×0.5	14.68	4644	60.9	-19.24	1
ESO-LV 4000370	SBc	5.9	1.8×0.9	14.47	2876	37.5	-18.40	1
ESO-LV 4880490	SBd	7.9	1.9×0.6	15.03	1870	25.0	-16.95	1
ESO-LV 5340200	Sb	3.1	0.9×0.3	16.19	17446	226.7	-20.58	1
PGC 26148	Sm	9.0	0.7×0.5	15.71	11718	156.2	-20.25	2
PGC 37759	Sc	6.0	0.6×0.4	15.89	14495	193.2	-20.54	2

3.2 Data reduction

The data reduction of the images and spectra was performed standard IRAF¹ routines.

After dark and bias subtraction, all the images were corrected for pixel-to-pixel intensity variations by using an average sky flat-

field frame for each night. The different images of each galaxy were shifted and aligned to an accuracy of a few hundredths of pixel using common field stars as reference. After checking that their point spread functions (PSFs) were comparable within a few percent, the images were combined to obtain a single image. The cosmic rays were identified during the combination process and removed using a sigma-clipping rejection algorithm. The sky background level was removed from the combined images by fitting a second-order polynomial to the regions free of sources. The median value of the residual sky level was determined in a large number of 5×5 pixel areas. These areas were selected in empty regions of the images,

¹ IRAF is distributed by the National Optical Astronomy Observatories which are operated by the Association of Universities for Research in Astronomy under cooperative agreement with the National Science Foundation.

free of objects and far from the galaxy. The mean of these median values was zero, as expected. For the error in the sky determination we adopted half of the difference between the maximum and minimum of the median values obtained in the sampled areas. For each combined image the photometric zero-point was derived using the Sloan Digital Sky Survey (SDSS) r -band magnitude of several stars present in the field of view. The total r -band magnitude of each galaxy is consistent within 0.1 mag with the value quoted in SDSS Data Release 7 (Abazajian et al. 2009).

After bias subtraction, the flatfield correction of the spectra was performed by means of quartz lamp spectra. They were normalised and divided into all the galaxy and star spectra, to correct for pixel-to-pixel sensitivity variations and large-scale illumination patterns due to slit vignetting. The cosmic rays were identified by comparing the photon counts in each pixel with the local mean and standard deviation and eliminated by interpolating over a suitable value. The residual cosmic rays were eliminated by manually editing the spectra. Each spectrum was rebinned using the wavelength solution obtained from the corresponding arc-lamp spectrum. We checked that the wavelength rebinning had been done properly by measuring the difference between the measured and predicted wavelengths of about 20 of unblended arc-lamp lines which were distributed over the whole spectral range of a wavelength-calibrated spectrum. The resulting accuracy in the wavelength calibration is better than 4 km s^{-1} . All the spectra were corrected for CCD misalignment and the flux calibrated using the sensitivity function from the spectrophotometric star spectrum of the corresponding night. The spectra obtained for the same galaxy in the same position were co-added using the centre of the stellar continuum as reference. This allowed to improve the signal-to-noise ratio (S/N) of the resulting two-dimensional spectrum. In such a spectrum, the contribution of the sky was determined by interpolating a one-degree polynomial along the outermost 20 arcsec at the two edges of the slit, where the galaxy light was negligible, and then subtracted. A sky subtraction better than 1 per cent was achieved.

3.3 Two-dimensional photometric decomposition

The photometric decomposition of the r -band images of PGC 26148, and PGC 37759 was performed using the Galaxy Surface Photometry Two-Dimensional Decomposition (GASP2D) algorithm by Méndez-Abreu et al. (2008). The structural parameters of the galaxies were derived assuming the galaxy surface-brightness distribution to be the sum of the contributions of a Sérsic bulge, an exponential disc, and, if necessary, a Ferrers bar. Conventional bulge-disc decompositions using GASP2D have been explored in detail in Pizzella et al. (2008) and Morelli et al. (2008). For sake of clarity, here we briefly describe the main properties of the bar component adopted in GASP2D.

We adopted the projected surface density of a three-dimensional Ferrers ellipsoid (Ferrers 1877) to describe the surface-brightness profile of the bars

$$I_{\text{bar}}(r) = I_{0,\text{bar}} \left[1 - \left(\frac{r_{\text{bar}}}{a_{\text{bar}}} \right)^2 \right]^{n_{\text{bar}}+0.5} \quad r_{\text{bar}} \leq a_{\text{bar}}, \quad (1)$$

where $I_{0,\text{bar}}$, a_{bar} , and n_{bar} represent the central surface-brightness, length, and shape parameter of bar, respectively. Due to the high degree of degeneracy that n_{bar} introduces in the fit, we decided to keep it as a fixed parameter ($n_{\text{bar}} = 2$ Laurikainen et al. (2005)) during the fitting process. All the bar models were built up in a frame of generalized ellipses (Athanasoula 1990). Thus, the bar reference system is defined as

$$r_{\text{bar}} = \frac{[(-(x-x_0) \sin \text{PA}_{\text{bar}} + (y-y_0) \cos \text{PA}_{\text{bar}})^c - ((x-x_0) \cos \text{PA}_{\text{bar}} + (y-y_0) \sin \text{PA}_{\text{bar}})^c]}{q_{\text{bar}}^c}]^{1/c}, \quad (2)$$

where q_{bar} and PA_{bar} are the axis ratio and position angle of the bar, respectively. The parameter c controls the shape of the isophotes. A value of $c = 2$ corresponds to a perfect ellipse, $c > 2$ to a boxy shape and $c < 2$ to a discy shape (see Aguerri et al. 2009, for more details).

To derive the photometric parameters of the bulge (effective surface brightness I_e , effective radius r_e , shape parameter n , major-axis position angle PA_b , and axial ratio q_b) and disc (central surface brightness I_0 , scalelength h , major-axis position angle PA_d , and axial ratio q_d) and the position of the galaxy centre (x_0, y_0) we fitted iteratively a model of the surface brightness $I_m(x, y) = I_b(x, y) + I_d(x, y)$ to the pixels of the galaxy image, using a non-linear least-squares minimisation based on the robust Levenberg-Marquardt method by Moré et al. (1980). The actual computation was done using the MPFIT (Markwardt 2009) under the IDL² environment. Each image pixel was weighted according to the variance of its total observed photon counts due to the contribution of both the galaxy and sky, and determined assuming photon noise limitation and taking into account for the detector read-out noise. The seeing effects were taken into account by convolving the model image with a circular Gaussian PSF with the FWHM measured from the field stars in the galaxy image. The convolution was performed as a product in Fourier domain before the least-squares minimisation.

The parameters derived for the structural components of the sample galaxies are collected in Table 2. The result of the photometric decomposition of the surface-brightness distribution of the analyzed galaxies is shown in Fig. 2.

Since the formal errors obtained from the χ^2 minimisation are not representative of the real errors in the structural parameters, a series of Monte Carlo simulations was performed to derive a reliable estimation of the errors. It was generated a set of barred and unbarred galaxies with a total r -band magnitude within $14.5 \leq M_T \leq 15.5$ mag. The structural parameters of the artificial galaxies were randomly chosen in the ranges

$$0.7 \leq r_e \leq 17 \text{ kpc}; 0.3 \leq q_b \leq 0.7; 0.5 \leq n \leq 12.5; \quad (3)$$

for the Sérsic bulges,

$$5 \leq h \leq 7 \text{ kpc}; 0.5 \leq q_d \leq 0.8; \quad (4)$$

for the exponential discs, and

$$0.5 \leq r_{\text{bar}} \leq 10 \text{ kpc}; 0.2 \leq q_{\text{bar}} \leq 0.7 \text{ with } q_{\text{bar}} \leq q_d \leq q_b; \quad (5)$$

for the Ferrers bar. The artificial galaxies were assumed to be observed at a distance of 194 Mpc taking into account for resolution effects. Finally, a background level and photon noise were added to the simulated images in order to mimic the instrumental setup and S/N of the actual observations. The artificial and observed galaxies were divided in bins of Sérsic index of width $\Delta n = 2$. The relative errors in the fitted parameters of the artificial galaxies were estimated by comparing the input and output values and were assumed to be normally distributed. The standard deviation

² The Interactive Data Language is distributed by ITT Visual Information Solutions.

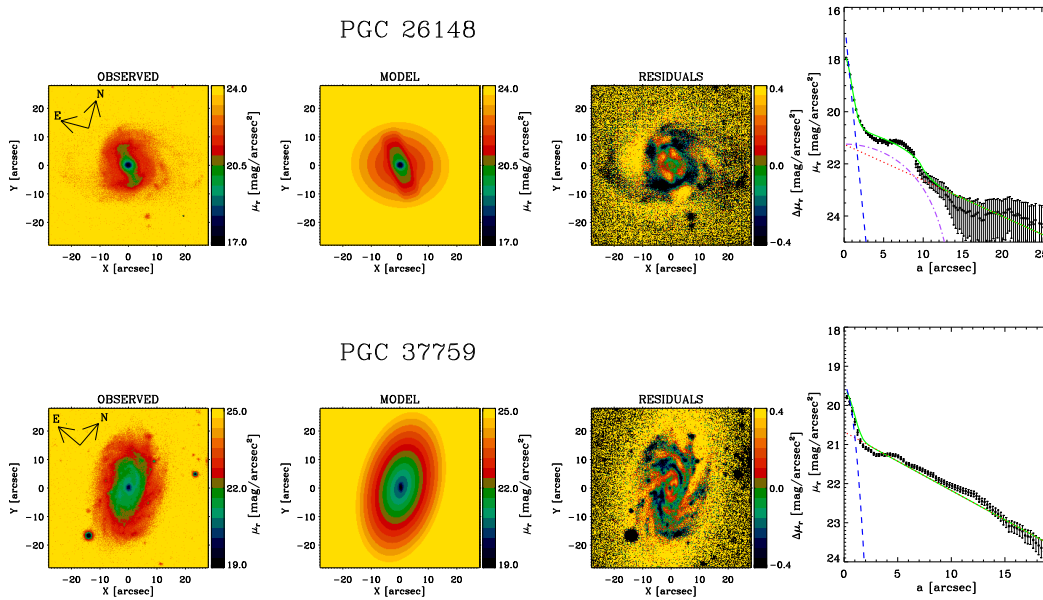


Figure 2. Two-dimensional photometric decomposition of PGC 26148 (top panel) and PGC 37759 (bottom panel). The FORS2 r -band image, best-fit image, residual (i.e., observed-model) image, and surface-brightness radial profile are shown (from left to right panel). In the right-hand panel the ellipse-averaged radial profile of the surface brightness measured in the FORS2 (dots) and model image (green continuous line) are shown. The dashed blue, dash-dotted purple line, and dotted red lines represent the intrinsic surface-brightness radial profiles of the bulge, bar, and disc, respectively.

Table 2. Photometric parameters of the bulge and disc of PGC 26148 and PGC 37759. The columns show the following. Column (2) the effective surface brightness of the bulge; column (3): effective radius of the bulge; column (4): shape parameter of the bulge; column (5): axial ratio of the bulge isophotes; column (6): position angle of the bulge major axis; column (7): central surface brightness of the disc; column (8): scale length of the disc; column (9): axial ratio of the disc isophotes; column (10): position angle of the disc major axis; column (11): Central surface brightness of the bar; column (12): radius of the bar; column (13): shape parameter of the bar; column (14): axial ratio of the bar isophotes; column (15): bulge-to-total luminosity ratio.

Galaxy	μ_e (mag/arcsec ²)	r_e (arcsec)	n	q_b	PA_b ($^\circ$)	μ_0 (mag/arcsec ²)	h (arcsec)	q_d	PA_d ($^\circ$)
(1)	(2)	(3)	(4)	(5)	(6)	(7)	(8)	(9)	(10)
					μ_{bar} (mag/arcsec ²)	r_{bar} (arcsec)	n_{bar}	q_{bar}	B/T
					(11)	(12)	(13)	(14)	(15)
PGC 26148	18.19 ± 0.29	0.56 ± 0.10	1.04 ± 0.05	0.81 ± 0.01	96.4 ± 2.0 21.24 ± 0.30	21.25 ± 0.03 14.64 ± 0.37	7.86 ± 0.16 2.00	0.86 ± 0.02 0.35 ± 0.04	98.3 ± 5.0 0.11
PGC 37759	20.23 ± 0.28	0.76 ± 0.11	0.50 ± 0.05	0.36 ± 0.03	44.2 ± 2.0 —	20.68 ± 0.20 —	7.24 ± 0.58 —	0.51 ± 0.03 —	27.3 ± 5.0 0.02

was adopted as the typical error in the relevant parameter for the bulge-disc decomposition of the observed galaxies (Table 2).

The face-on central surface brightness of the disc in the B band $\mu_{0,B}^0$ was obtained from the r -band μ_0 (Table 2) by correcting for galaxy inclination and adopting a $B - r$ color which was computed from $g - r$ measured on the SDSS images at $r \geq r_e$ and transformed to B band according to Chonis & Gaskell (2008). It is $B - r = 1.20$ for PGC 26148 and $B - r = 1.21$ for PGC 37759, and therefore $\mu_{0,B}^0 = 22.61$ and $\mu_{0,B}^0 = 22.62$ mag/arcsec² respectively.

3.4 Stellar kinematics

The stellar kinematics was measured from the galaxy absorption features present in the wavelength range centred on the H_β (λ 4861 Å) line and Mg I line triplet ($\lambda\lambda$ 5164, 5173, 5184 Å) by applying

the Penalized Pixel Fitting (pPXF, Cappellari & Emsellem 2004) and Gas AND Absorption Line Fitting (GANDALF, Sarzi et al. 2006) IDL packages adapted for dealing with the FORS2 spectra.

The galaxy spectra were rebinned along the dispersion direction to a logarithmic scale, and along the spatial direction to obtain a $S/N \geq 40$ per resolution element. It is $S/N \simeq 20$ per resolution element at the outermost radii only.

At each radius a linear combination of template stellar spectra from the ELODIE library by Prugniel & Soubiran (2001) was convolved with the line-of-sight velocity distribution (LOSVD) and fitted to the observed galaxy spectrum by χ^2 minimization in pixel space. The LOSVD was assumed to be a Gaussian plus third- and fourth-order Gauss-Hermite polynomials \mathcal{H}_3 and \mathcal{H}_4 , which describe the asymmetric and symmetric deviations of the LOSVD from a pure Gaussian profile (van der Marel & Franx 1993; Gerhard 1993). This allowed us to derive profiles of the line-

of-sight velocity (v), velocity dispersion (σ), and third- (h_3) and fourth-order (h_4) Gauss-Hermite moments of the stars. The spectral resolution of the template stellar spectra (FWHM = 0.5 Å) was degraded to match the spectral resolution of our galaxy spectra. The stellar spectra were convolved with a Gaussian before measuring the galaxy kinematics. Bad pixels coming from imperfect subtraction of cosmic rays and sky emission lines were properly masked and excluded from the fitting procedure. Ionized-gas emission lines were simultaneously fitted as Gaussians and a low-order additive Legendre polynomial was added to correct for the different shape between the galaxy and template spectra. The uncertainties on the kinematic parameters were estimated from the formal errors after rescaling to have a reduced $\chi^2 = 1$. The measured stellar kinematics is reported in Table A1, where the line-of-sight velocities are relative to the galaxy centre. The folded kinematic profiles are plotted in Fig. 3.

The rotation curve along the major axis of PGC 26148 is characterized by negative values ($v \simeq -10 \text{ km s}^{-1}$) in the innermost 1 arcsec, where the velocity dispersion shows a decrease and h_4 peaks to 0.1. Further out, the rotation velocity increases to a maximum $v \simeq 20 \text{ km s}^{-1}$ at 4 arcsec and then decreases to zero at the last observed radius. This waving pattern in the rotation curve has been detected in several barred galaxies (Bettoni & Galletta 1997) and it is due to the presence of retrograde orbits (Wozniak & Pfenniger 1997).

PGC 37759 shows a regular kinematics. The rotation velocity reaches a maximum of about 140 km s^{-1} at about 8 arcsec from the centre and it remains constant at larger radii. No rotation is observed along the minor axis. The velocity dispersion is about 70 km s^{-1} in the centre and decreases to 40 km s^{-1} outwards. The Gauss-Hermite moments are $h_3 \simeq 0$ and $h_4 \simeq 0$ at all radii.

3.5 Line-strength indices

The Mg, Fe, and H_β line-strength indices as defined by Faber et al. (1985) and Worthey et al. (1994) were measured from the flux calibrated spectra of the 8 sample galaxies following Morelli et al. (2004, 2008). The average Iron index $\langle \text{Fe} \rangle = (\text{Fe}5270 + \text{Fe}5335)/2$ (Gorgas et al. 1990) and the combined Magnesium-Iron index $[\text{MgFe}]' = \sqrt{\text{Mg} b (0.72 \times \text{Fe}5270 + 0.28 \times \text{Fe}5335)}$ (Thomas et al. 2003) were measured too.

The difference between the spectral resolution of the galaxy spectra and the Lick/IDS system one (FWHM = 8.4 Å; Worthey & Ottaviani 1997) was taken into account by degrading our spectra through a Gaussian convolution to match the Lick/IDS resolution before measuring the line-strength indices. No focus correction was applied because the atmospheric seeing was the dominant effect during observations (see Mehlert et al. 1998, for details). The errors on the line-strength indices were derived from photon statistics and CCD read-out noise, and calibrated by means of Monte Carlo simulations.

The contamination of the H_β line-strength index by the H_β emission line due to the ionized gas present in the galaxy is a problem when deriving the properties of the stellar populations. Indeed, if the H_β emission fills the absorption line and a proper separation of both contributions is not performed before the analysis, the measured ages result to be artificially older. To address this issue the H_β index was measured from the galaxy spectrum after subtracting the contribution of the H_β emission line. Only H_β emission

lines detected with a $S/N > 3$ were subtracted from the observed spectra.

The original Lick/IDS spectra are not flux calibrated contrary to ours. Such a difference in the continuum shape could introduce small systematic offsets of the measured values of the indices. To derive these offsets and to calibrate our measurements to the Lick/IDS system, the values of the line-strength indices measured for a sample of templates were compared to those obtained by Worthey et al. (1994). The spectra of the template stars were obtained with the same setup as our galaxy spectra and were retrieved from ESO Science Archive. The offsets were evaluated as the mean of the differences between our and Lick/IDS line-strength values. They were neglected being smaller than the mean error of the differences. Therefore, no offset correction was applied to our line-strength measurements.

The measured values of H_β , $[\text{MgFe}]'$, $\langle \text{Fe} \rangle$, Mg_b , and Mg_2 for all the sample galaxies are listed in Table A2 and plotted in Fig. 4.

4 PROPERTIES OF THE STELLAR POPULATIONS

4.1 Central values of the line-strength indices

In Paper I the central values of velocity dispersion was obtained by a weighted mean of all the measured data points within an aperture of radius $0.3 r_e$ along all the available spectra. The adopted weight for each data point was proportional to the S/N of the spectrum extracted along the spatial direction where the kinematics measurement was performed. Similarly, the central value of σ for PGC 26148 and PGC 37759, and of Mg_b , Mg_2 , H_β , $\langle \text{Fe} \rangle$, and $[\text{MgFe}]'$ for all the sample galaxies were obtained in this paper. They are listed in Tab. 3.

Fig. 5 shows the correlations between the central values of velocity dispersion and those of Mg_2 , H_β , and $\langle \text{Fe} \rangle$. They are compared with the results obtained by Morelli et al. (2008) for a sample of bulges hosted by HSB discs. Usually, Mg_2 is adopted as the tracer of the α elements and gives an estimate of the $[\alpha/\text{Fe}]$ enhancement, while σ is related to the gravitational potential and, therefore, is a proxy of the mass. For early-type galaxies and bulges the Mg_2 - σ correlation shows that more massive systems host a more metal-rich stellar population (see Idiart et al. 1996; Bernardi et al. 1998; Jørgensen 1999a; Mehlert et al. 2003; Morelli et al. 2008). We find that the bulges of LSB galaxies follow a Mg_2 - σ relationship which is remarkably similar to that of their HSB counterparts (e.g. Ganda et al. 2007; Morelli et al. 2008). Theoretical models of galaxy formation through dissipative collapse predict a tight $\langle \text{Fe} \rangle$ - σ correlation (e.g., Kodama et al. 1998), which is observed for bulges of spiral galaxies (Idiart et al. 1996; Prugniel et al. 2001; Proctor & Sansom 2002; Morelli et al. 2008) but not for early-type galaxies (Fisher et al. 1996; Jørgensen 1999a; Trager et al. 1998; Mehlert et al. 2003). The slope and zero-point of the $\langle \text{Fe} \rangle$ - σ relation of the bulges of LSB and in HSB galaxies (Morelli et al. 2008) are consistent within errors. We measure an anti-correlation between H_β and σ for the bulges in LSB galaxies. It suggests that less massive bulges host younger stellar populations with respect to more massive ones. In spite of the large scatter of the data points, the measured trend is in good agreement with the measurements obtained by Ganda et al. (2007) and Morelli et al. (2008) for bulges in HSB galaxies.

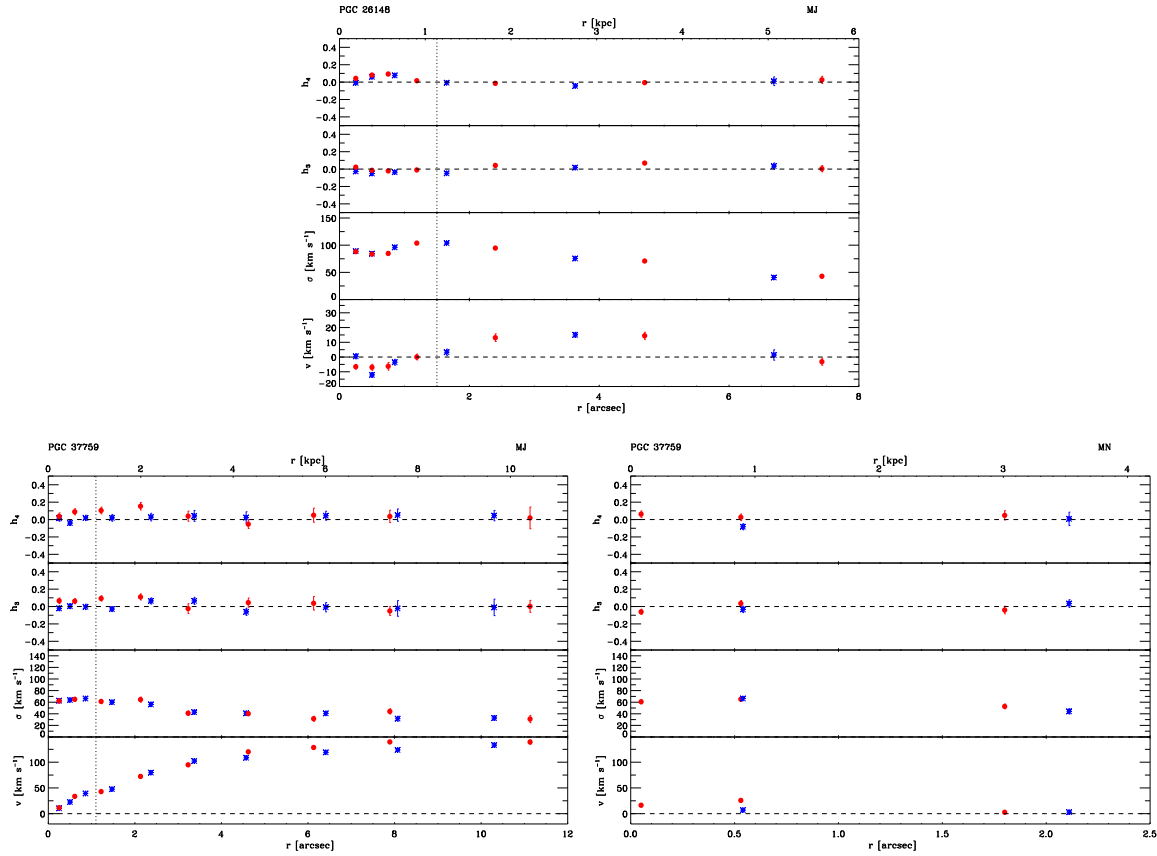


Figure 3. Stellar kinematics measured along the major axis of PGC 26148 and along the major and minor axes of PGC 37759. For each axis the curves are folded around the nucleus. Asterisks and dots refer to data measured along the approaching and residing side of the galaxy, respectively. The radial profiles of the line-of-sight velocity (v) after the subtraction of the systemic velocity, velocity dispersion (σ), third, and fourth order coefficients of the Gauss-Hermite decomposition of the LOSVD (h_3 and h_4) are shown (from top to bottom panel). The vertical dashed line corresponds to the radius r_{bd} where the surface-brightness contributions of the bulge and disc are equal.

Table 3. Central values of the velocity dispersion and line-strength indices of the sample galaxies measured within an aperture of radius $0.3 r_e$. Column (8) gives the source of the spectrum measured in this paper and the reference for r_e and σ : 1 = Paper I, 2 = this paper.

Galaxy	σ (km s^{-1})	$\langle \text{Fe} \rangle$ (\AA)	$[\text{MgFe}]'$ (\AA)	Mg_2 (mag)	Mg_b (\AA)	H_β (\AA)	Source
(1)	(2)	(3)	(4)	(5)	(6)	(7)	(8)
ESO-LV 1860550	91.7 ± 2.0	2.53 ± 0.09	2.97 ± 0.01	0.206 ± 0.003	3.40 ± 0.09	2.01 ± 0.10	1
ESO-LV 2060140	54.3 ± 2.0	1.80 ± 0.23	1.92 ± 0.05	0.111 ± 0.007	1.96 ± 0.20	3.68 ± 0.23	1
ESO-LV 2340130	64.1 ± 2.0	1.28 ± 0.11	1.39 ± 0.01	0.089 ± 0.003	1.49 ± 0.11	3.94 ± 0.14	1
ESO-LV 4000370	42.0 ± 2.5	1.68 ± 0.24	1.76 ± 0.04	0.092 ± 0.006	1.78 ± 0.20	2.64 ± 0.22	1
ESO-LV 4880490	48.2 ± 2.5	1.10 ± 0.26	1.06 ± 0.03	0.047 ± 0.006	1.02 ± 0.19	3.57 ± 0.24	1
ESO-LV 5340200	153.9 ± 7.0	2.47 ± 0.12	2.80 ± 0.02	0.183 ± 0.004	3.14 ± 0.10	2.86 ± 0.11	1
PGC 26148	93.1 ± 1.6	2.41 ± 0.14	2.59 ± 0.02	0.149 ± 0.003	2.73 ± 0.11	2.62 ± 0.10	2
PGC 37759	64.4 ± 3.1	2.63 ± 0.23	2.97 ± 0.07	0.119 ± 0.006	3.17 ± 0.20	2.50 ± 0.18	2

4.2 Central values of the age, metallicity, and α/Fe enhancement

The models by Thomas et al. (2003) predict the values of the line-strength indices for a single stellar population as function of the age, metallicity, and $[\alpha/\text{Fe}]$ ratio. In the top panel of Fig. 6 the

central values of H_β and $[\text{MgFe}]'$ are compared with the model predictions by Thomas et al. (2003) for two stellar populations with solar ($[\alpha/\text{Fe}] = 0$ dex) and super-solar α/Fe enhancement ($[\alpha/\text{Fe}] = 0.5$ dex), respectively. In this parameter space the mean age and total metallicity appear to be almost insensitive to the variations of the α/Fe enhancement. In the bottom panel of Fig. 6 the

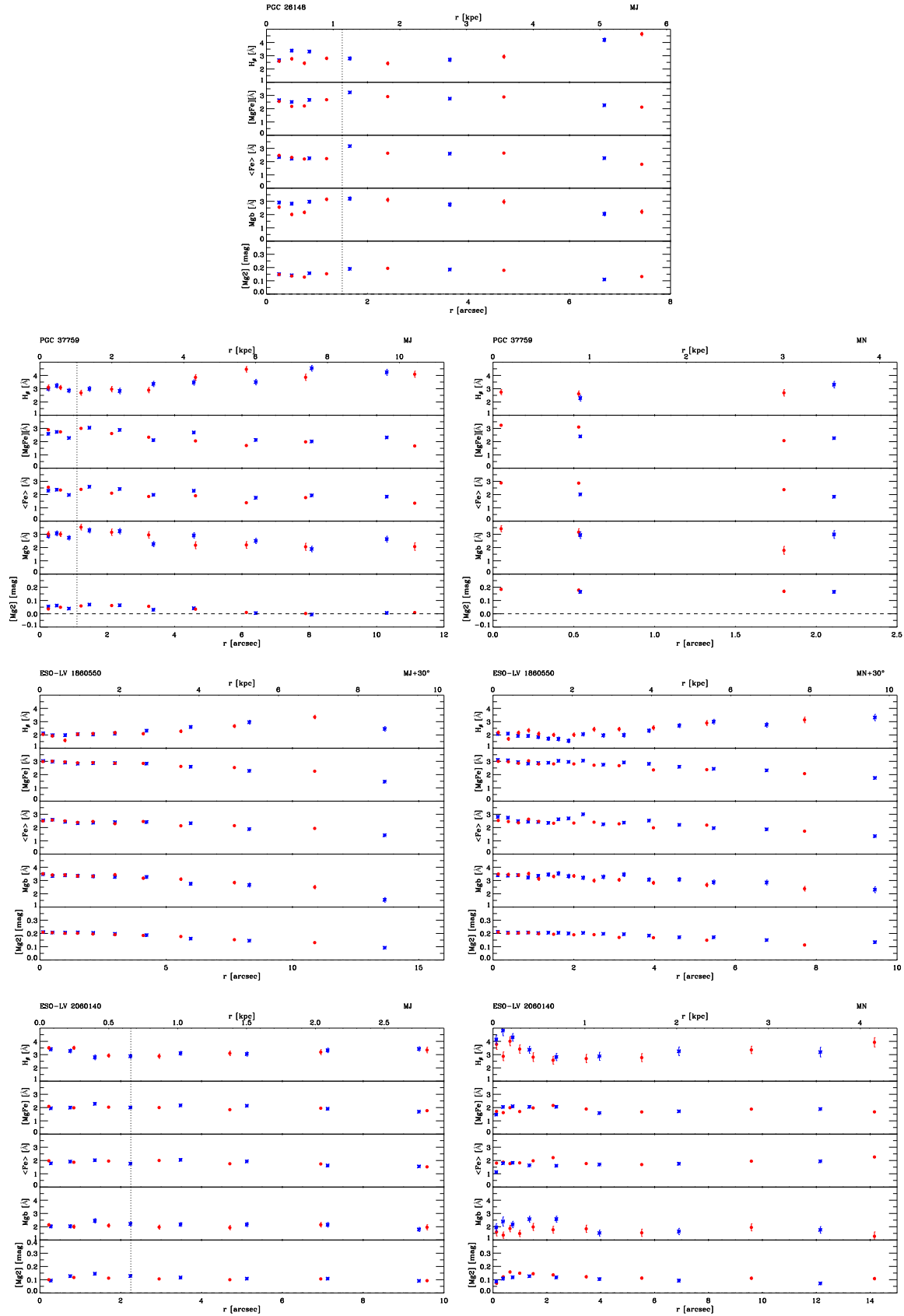


Figure 4. Line-strength indices measured along the available axes of the sample galaxies. For each axis the curves are folded around the nucleus. Asterisks and dots refer to data measured along the approaching and residing side of the galaxy, respectively. The radial profiles of the line-strength indices H_β , $[MgFe]'$, $\langle Fe \rangle$, Mg_b , and Mg_2 are shown (from top to bottom panel). The vertical dashed line corresponds to the radius r_{bd} where the surface-brightness contributions of the bulge and disc are equal. For each dataset the name of the galaxy and the location of the slit position (Mj=major axis, MN=minor axis) are given.

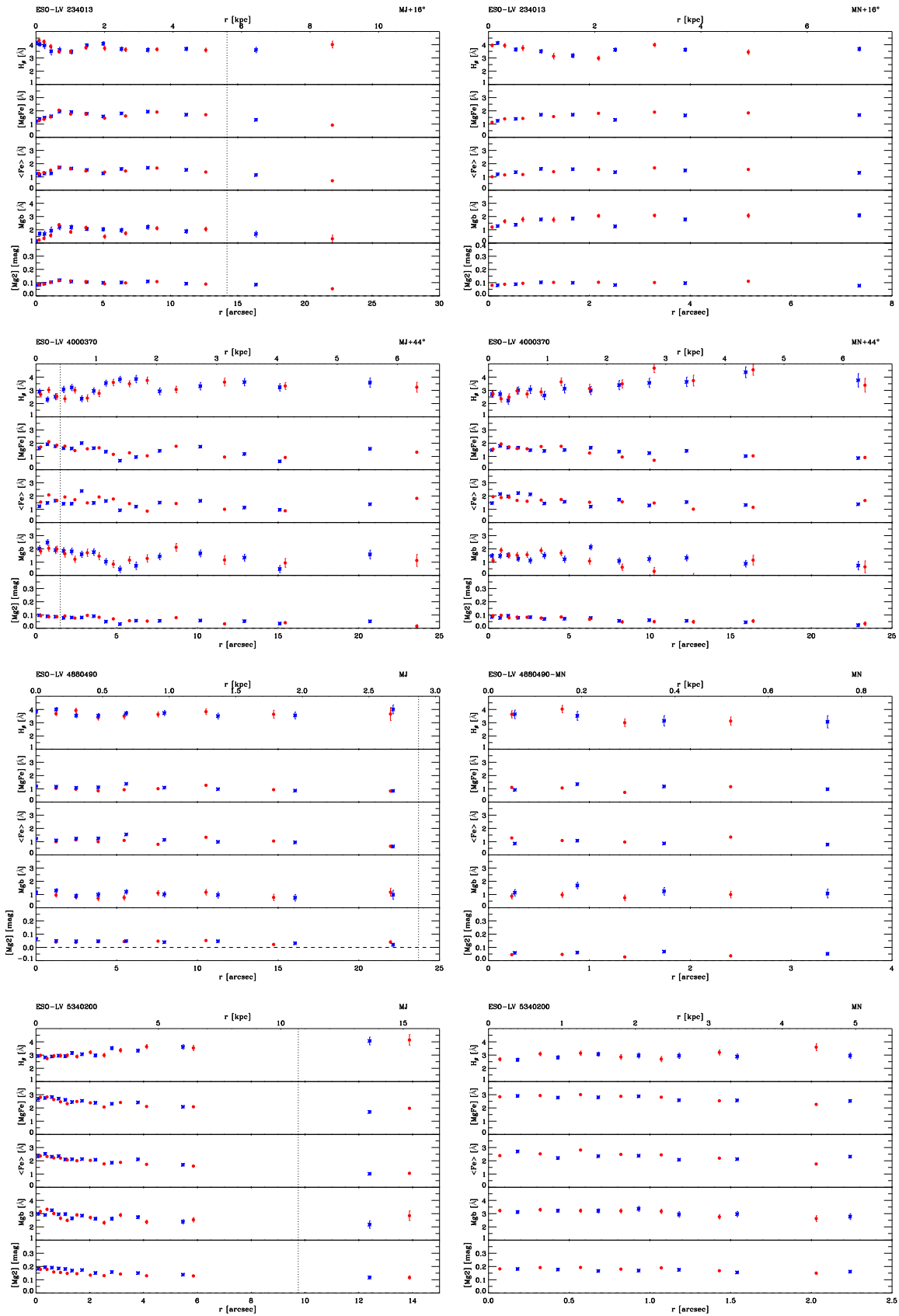


Figure 4 – continued

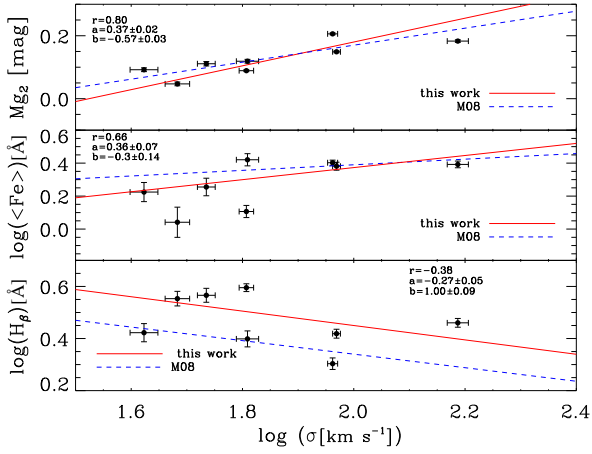


Figure 5. Central values of the line-strength indices Mg_2 (upper panel), $\langle Fe \rangle$ (central panel), and H_β (lower panel) as a function of the central velocity dispersion. In each panel the red solid line and blue dashed line represent the linear regression ($y = ax + b$) through the data points and the correlation found by Morelli et al. (2008) for bulges of HSB galaxies, respectively. The Pearson correlation coefficient (r) and the coefficients of the linear fit are given.

Table 4. Mean age, total metallicity, and total α/Fe enhancement of the stellar populations of the bulges of the sample galaxies

Galaxy	Age [Gyr]	$[Z/H]$	$[\alpha/Fe]$
(1)	(2)	(3)	(4)
ESO-LV 1860550	4.9 ± 1.6	0.01 ± 0.06	0.11 ± 0.06
ESO-LV 2060140	1.3 ± 0.2	-0.11 ± 0.07	0.06 ± 0.13
ESO-LV 2340130	1.2 ± 0.2	-0.53 ± 0.06	0.09 ± 0.09
ESO-LV 4000370	4.3 ± 1.4	-0.62 ± 0.09	-0.04 ± 0.12
ESO-LV 4880490	2.9 ± 1.0	-1.07 ± 0.09	-0.24 ± 0.20
ESO-LV 5340200	1.5 ± 0.1	0.31 ± 0.04	0.18 ± 0.06
PGC 26148	1.9 ± 0.2	0.08 ± 0.04	0.05 ± 0.06
PGC 37759	1.8 ± 0.6	0.29 ± 0.11	0.10 ± 0.11

central values of Mg_b and $\langle Fe \rangle$ are compared with the model predictions by Thomas et al. (2003) for two stellar populations with an intermediate (2 Gyr) and old age (6 Gyr), respectively. In this parameter space the total metallicity and total α/Fe enhancement appear to be almost insensitive to the variations of the age. The central mean age, total metallicity, and total α/Fe enhancement of the stellar population in the centre of the sample galaxies were derived from the values of line-strength indices given in Table 3 by a linear interpolation between the model points using the iterative procedure described in Mehlert et al. (2003) and Morelli et al. (2008). The derived values and their corresponding errors are representative of the properties of the stellar populations of the galaxy bulges and listed in Tab. 4. The histograms of their number distribution are plotted in Fig. 7.

All the bulges are characterized by a very young stellar population, with a distribution of ages peaked at the value of 1.5 Gyr. Only the bulges of ESO-LV 1860550 and ESO-LV 4000370 show an intermediate-age (4-5 Gyr) stellar population. The globally young nature of these objects is also suggested from the on-going star formation as shown by the presence of the H_β emis-

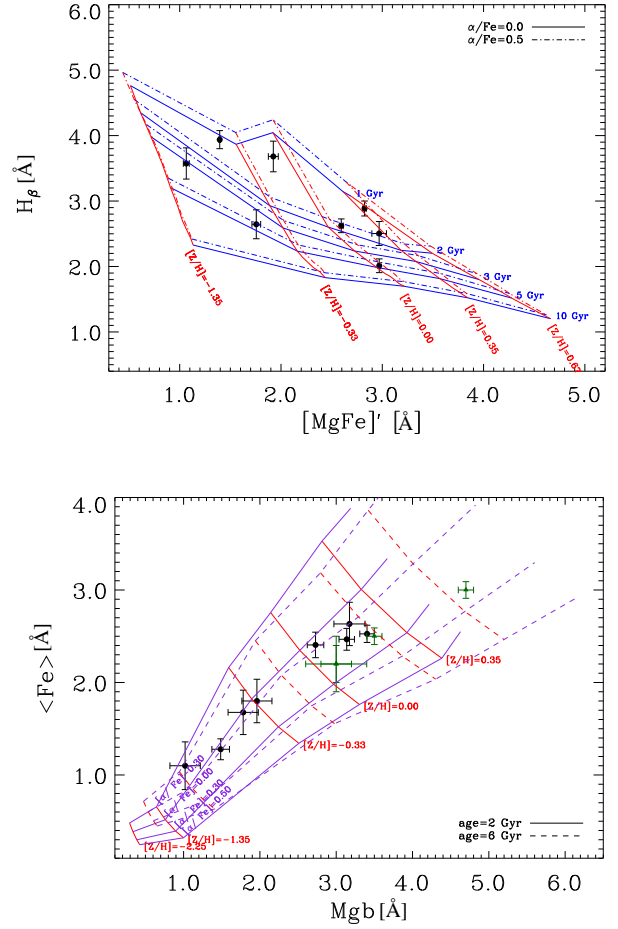


Figure 6. The distribution of the central values of H_β and $[MgFe]'$ indices (top panel) and $\langle Fe \rangle$ and Mg_b indices (bottom panel) measured over an aperture of $0.3 r_e$ for the sample galaxies. The lines indicate the models by Thomas et al. (2003). In the top panel the age-metallicity grids are plotted with two different α/Fe enhancements: $[\alpha/Fe] = 0.0$ dex (continuous lines) and $[\alpha/Fe] = 0.5$ dex (dashed lines). In the bottom panel the $[\alpha/Fe]$ ratio-metallicity grids are plotted with two different ages: 2 Gyr (continuous lines) and 6 Gyr (dashed lines). Green triangles are the values obtained for 3 LSB galaxies by Bergmann et al. (2003).

sion line in their spectra. This result confirms the presence of young stars in LSB galaxies as previously reported from spectroscopic (Bergmann et al. 2003; Zhong et al. 2010) and photometric (Galaz et al. 2002; Zackrisson et al. 2005; Galaz et al. 2006; Vorobyov et al. 2009; Galaz et al. 2011) analysis of the stellar populations. Even though the number of sample galaxies does not allow us to trace a firm statistical conclusion, it is interesting to note that we do not find any old-age bulge in LSB discs (Fig. 7, left-hand panel), whereas they were approximately 25 per cent in the HSB sample studied with the same technique by Morelli et al. (2008) which is similar to our sample for both mass range and morphological type. The metallicity of the bulges of LSB discs spans a large range of values from high ($[Z/H] = 0.30$ dex) to sub-solar metallicity ($[Z/H] = -1.0$ dex) with an almost flat distribution (Fig. 7, middle panel). The obtained ages and metallicity well match the $B - r$ colour (or $B - R$ given in Paper I) derived for the sample galaxies.

Most of the sample bulges display solar α/Fe enhancements

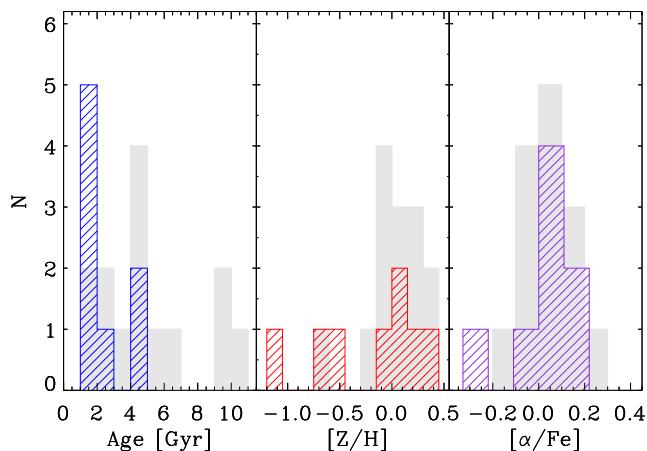


Figure 7. Distribution of the mean age (left-hand panel), total metallicity (central panel), and total α/Fe enhancement (right-hand panel) for the stellar populations of the bulges of the sample galaxies. The distribution of the same quantities obtained by Morelli et al. (2008) for the bulges of HSB discs are plotted in grey for sake of comparison.

(Fig. 7, right-hand panel). The number distribution has a median at $[\alpha/\text{Fe}] = 0.09$ and spreads from super ($[\alpha/\text{Fe}] = 0.3$) to sub-solar values ($[\alpha/\text{Fe}] = -0.2$). These values are consistent with those obtained for the 3 LSB galaxies studied by Bergmann et al. (2003) and plotted for comparison in Fig. 6. They are also remarkably similar to the $[\alpha/\text{Fe}]$ ratios derived for the bulges of HSB galaxies (Morelli et al. 2008) and for elliptical galaxies in clusters (Peletier 1989; Jørgensen 1999b; Trager et al. 2000; Kuntschner 2000; Kuntschner et al. 2001). They imply a star-formation time-scale ranging from less than 1 to 5 Gyr in agreement with the predictions of most of the models of bulge formation (Gilmore & Wyse 1998; Elmegreen et al. 2008; Cescutti & Matteucci 2011).

The correlation between the galaxy morphological type and the properties of the bulge stellar population is indicative of the possible interplay between the evolution of bulge and disc. Thomas & Davies (2006) did not observe any correlation between the age and metallicity of the bulge stellar population and galaxy morphology, whereas Ganda et al. (2007) and Morelli et al. (2008) found a mild correlation with the early-type galaxies ($T < 0$) being older and more metal rich than spiral galaxies ($T \geq 0$). Since the above relationships are mostly driven by the early-type galaxies which are lacking in our sample, we do not observe any correlation between the galaxy morphological type ($2 \leq T \leq 9$) and the age, metallicity, or α/Fe enhancement of our bulges (Fig. 8). Nevertheless, we can exclude a strong interplay between the bulge and disc components.

Despite their different distributions, metallicity and α/Fe enhancement are strongly correlated, as shown in Fig. 9. This implies that the last episode of star formation was very short in galaxies with high metallicities, whereas it lasts longer in galaxies with low metallicity. A similar trend was also found for the bulges of HSB galaxies (Morelli et al. 2008) and for early-type galaxies (Spolaor et al. 2010). We do not find any correlation between age and metallicity or α/Fe enhancement (Fig. 9).

In early-type galaxies (Mehlert et al. 2003; Denicoló et al. 2005; Thomas et al. 2005; Sánchez-Blázquez et al. 2006; Annibaldi et al. 2007; MacArthur et al. 2009; Spolaor et al. 2010) and in bulges of HSB galaxies (Ganda et al. 2007; Morelli et al.

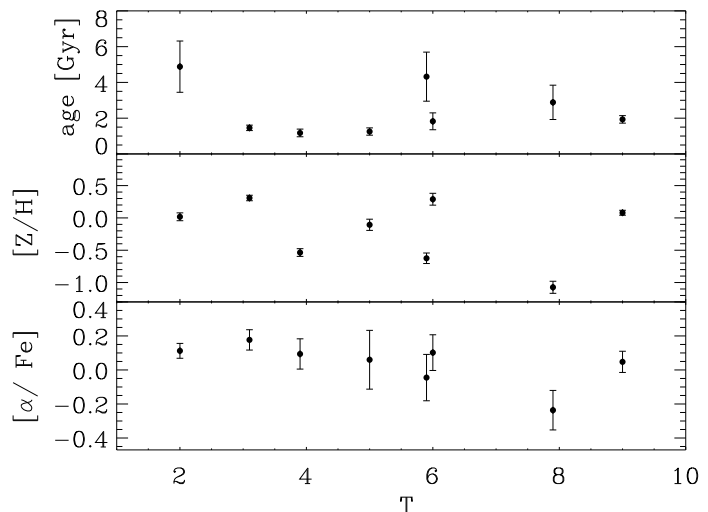


Figure 8. Mean age (upper panel), total metallicity (middle panel), and total α/Fe enhancement (lower panel) of the stellar populations of the bulges of the sample galaxies as a function of galaxy morphological type.

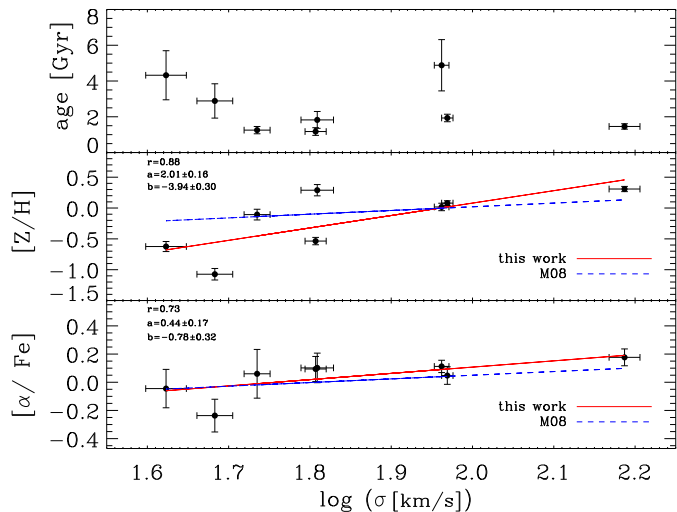


Figure 10. Mean age (upper panel), total metallicity (middle panel), and total α/Fe enhancement (lower panel) of the stellar populations of the bulges of the sample galaxies as a function of the central velocity dispersion. In each panel the red solid line and blue dashed line represent the linear regression ($y = ax + b$) through the data points and the correlation found by Morelli et al. (2008) for bulges of HSB galaxies, respectively. The Pearson correlation coefficient (r) and the coefficients of the linear fit are given.

2008) the metallicity and α/Fe enhancement are well correlated with the central velocity dispersion. Metallicity and α/Fe enhancement of bulges of LSB galaxies correlate with velocity dispersion (Fig. 10) and the correlation is consistent with the results obtained in Morelli et al. (2008). These relations are explained by chemodynamical models (Matteucci 1994; Kawata & Gibson 2003; Kobayashi 2004) and cosmological hydrodynamic simulations (De Lucia et al. 2004; Tassis et al. 2008) of ellipticals and bulges as the result of a mass-dependent star formation efficiency. Indeed, low-mass galaxies have a lower efficiency in converting gas-phase metals into new stars and this gives rise to a prolonged star formation and to lower α/Fe ratios. Our results suggest that this is true also for the bulges of LSB galaxies. We conclude the most massive bulges of our sample galaxies are more metal rich,

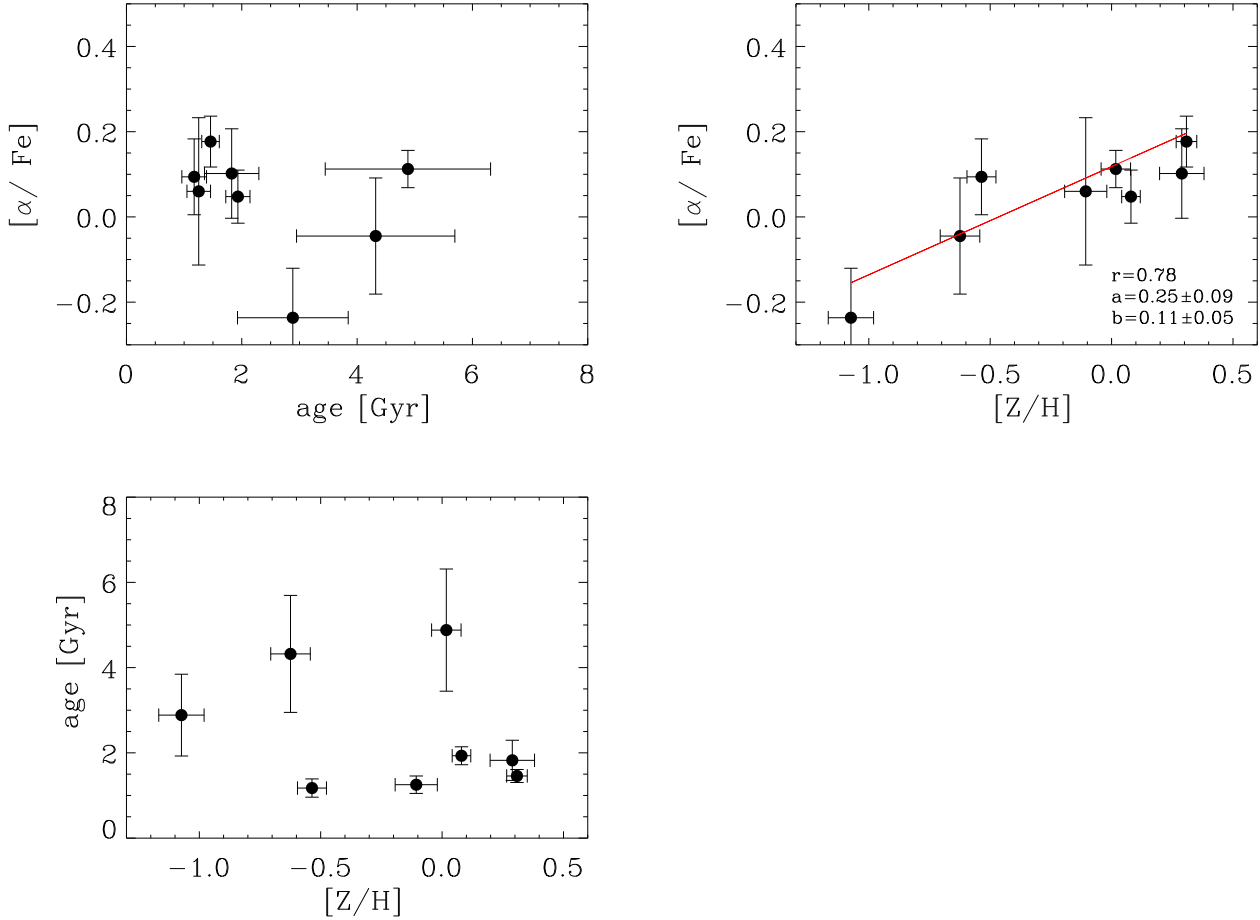


Figure 9. Mean age, total metallicity, and α/Fe enhancement of the stellar populations of the bulges of the sample galaxies. In the upper right-hand panel the red solid line represents the linear regression ($y = ax + b$) through the data points. The Pearson correlation coefficient (r) and the coefficients of the linear fit are given.

and characterized by a shorter star-formation time-scale. The relationship between the age and central velocity dispersion is more controversial. The presence of an age drop for low-mass galaxies ($\log \sigma < 2.1$) was pointed out by Nelan et al. (2005) and was observed also by Thomas et al. (2005), Morelli et al. (2008), and Spolaor et al. (2010). We do not find any correlation, but all our galaxies are in the low-mass regime, except for ESO-LV 5340200.

The case of bulge of ESO-LV 4880490 is particularly interesting. The central stellar population of this late-type barred spiral has an intermediate age (3 Gyr) and very low values of both metal content ($[Z/H] = -1.07$ dex) and α/Fe ratio ($[\alpha/\text{Fe}] = -0.24$ dex). This suggests a very prolonged star formation history in the galaxy centre consistent with a slow building up of the bulge within a scenario of secular evolution driven by the bar.

4.3 Radial gradients of the age, metallicity, and α/Fe enhancement

An issue in measuring the gradients of the age, metallicity, and α/Fe enhancement in bulges could be the contamination of their stellar population by the light coming from the underlying disc stellar component. This effect is negligible in the galaxy centres but it

could increase going to the outer regions of bulges, where the light starts to be dominated by the disc component. In order to reduce the impact of disc contamination and extend as much as possible the region in which deriving gradients, we map them inside r_{bd} , the radius where the bulge and disc give the same contribution to the total surface brightness (Morelli et al. 2008). Deriving gradients in the bulge dominated region with this approach will not remove completely the contamination by the disc stellar population, but it will assure always a similar degree of contamination in comparing the gradients of different galaxies.

For each galaxy, we derived the Mg_2 , H_β , and, $\langle \text{Fe} \rangle$ line-strength indices at the radius r_{bd} (Tab. 5). The corresponding ages, metallicities, and α/Fe enhancements were derived by using the stellar population models by Thomas et al. (2003) as done for the central values. The gradients of the properties of the bulge stellar population were derived from the values of age, metallicity, and α/Fe enhancement in the radial range out to r_{bd} . The errors on the gradients were calculated through Monte Carlo simulations taking into account the errors on the values out to r_{bd} . The final gradients of the age, metallicity, and α/Fe enhancement and their corresponding errors are listed in Tab. 5. The histograms of their number distribution are plotted in Fig. 11.

All the sample bulges show no age gradient within the er-

Table 5. Gradients of age, metallicity, and α /Fe enhancement of the stellar populations of the sample bulges derived from the central values and values at the radius r_{bd} where the surface-brightness contributions of the bulge and disc are equal

Galaxy	r_{bd} (arcsec)	$\Delta(\text{Age})$ [Gyr]	$\Delta([Z/H])$	$\Delta([\alpha/\text{Fe}])$
(1)	(2)	(3)	(4)	(5)
ESO-LV 1860550	16.2	2.01 ± 2.14	-0.05 ± 0.05	-0.06 ± 0.12
ESO-LV 2060140	2.2	-0.46 ± 0.26	0.10 ± 0.06	-0.03 ± 0.15
ESO-LV 2340130	14.2	-0.33 ± 0.85	-0.18 ± 0.13	-0.11 ± 0.19
ESO-LV 4000370	1.5	1.19 ± 1.96	-0.28 ± 0.12	0.13 ± 0.15
ESO-LV 4880490	23.3	-0.47 ± 1.50	0.07 ± 0.16	0.07 ± 0.25
ESO-LV 5340200	9.8	0.03 ± 0.18	0.15 ± 0.06	-0.02 ± 0.08
PGC 26148	1.5	0.78 ± 0.39	-0.22 ± 0.07	-0.45 ± 0.10
PGC 37759	1.1	0.57 ± 1.25	-0.13 ± 0.07	-0.07 ± 0.17

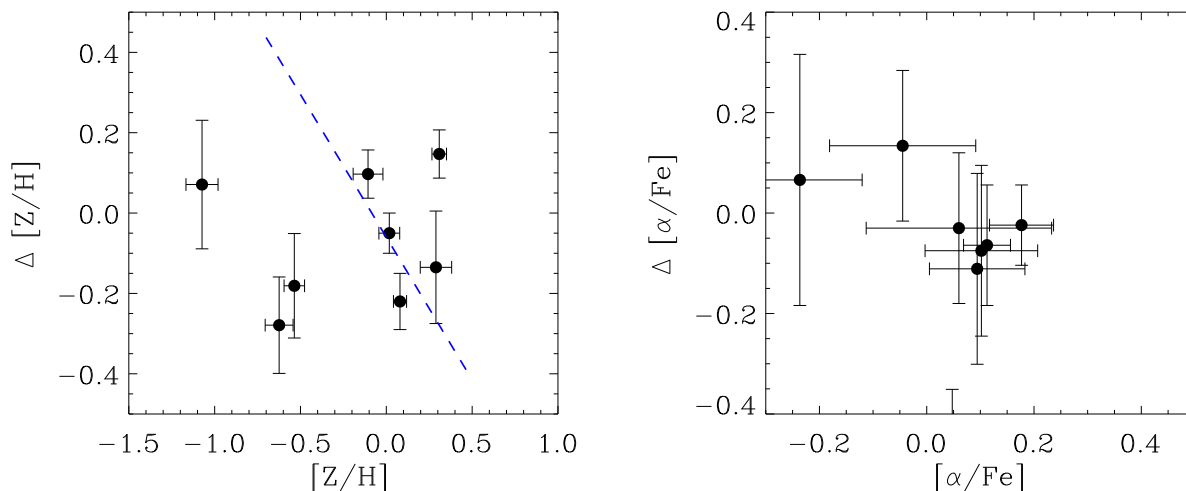


Figure 12. Gradient and central value of metallicity (left-hand panel) and α /Fe enhancement (right-hand panel) for the sample bulges. In the left-hand panel the dashed blue line represents the linear regression obtained for bulges of HSB galaxies by Morelli et al. (2008)

rorbars, except for ESO-LV 2060140 and PGC 26148 which are characterized by a shallow gradient. At face values the largest age gradients are measured for the bulges of ESO-LV 1860550, ESO-LV 4000370, ($\Delta(\text{age}) = 1 - 2$ Gyr, Fig. 11, left-hand panel), which are nevertheless consistent with $\Delta(\text{age}) = 0$ due to their large uncertainties (Tab. 5).

In spite of the peak at $\Delta([Z/H]) = -0.15$, the median of the number distribution of the metallicity gradients is consistent with $\Delta([Z/H]) = 0$ (Fig. 11, middle panel). Only ESO-LV 2340130, ESO-LV 4000370 and PGC 26148 host a bulge with a stellar population characterized by a metallicity gradient which is significantly negative (Tab. 5). Also the number distribution of the gradients of α /Fe enhancements has a median $\Delta([\alpha/\text{Fe}]) = 0$ (Fig. 11, right-hand panel). In all the observed distributions, most of the deviations from the median values can be explained as due only to the errors in the estimates of the gradients (Tab. 5).

The absence of significant age and α /Fe gradients is in agreement with the earlier findings for early-type galaxies (Mehlert et al. 2003; Sánchez-Blázquez et al. 2006; Spolaor et al. 2010) and bulges of unbarred (Jablonka et al. 2007; Morelli et al. 2008) and

barred (Sánchez-Blázquez et al. 2011; de Lorenzo-Cáceres et al. 2012) HSB galaxies. On the other hand, negative gradients of metallicity are observed in the radial profiles of many early-type galaxies (Proctor & Sansom 2002; Mehlert et al. 2003; Sánchez-Blázquez et al. 2006; Rawle et al. 2010) and bulges of HSB galaxies (Jablonka et al. 2007; Morelli et al. 2008).

In the models the presence of a negative metallicity gradient predicts a formation scenario of the bulges in LSB galaxies via dissipative collapse (Eggen et al. 1962; Larson 1974; Arimoto & Yoshii 1987) when a strong interplay between the star formation time-scale and gas flows is taken into account to explain of the absence of any α /Fe gradient (Pipino et al. 2008). But, pure dissipative collapse is not able to explain formation of all the sample bulges and other phenomena, like mergers or acquisition events, need to be invoked to account for the formation of those bulges which do not show any metallicity gradient (Bekki & Shioya 1999; Kobayashi & Arimoto 1999).

The metallicity gradients are plotted as a function of the metallicity in the galaxy centre in the left-hand panel of Fig. 12. Only the bulges of LSB galaxies with higher metallicity ($-0.1 < [Z/H] <$

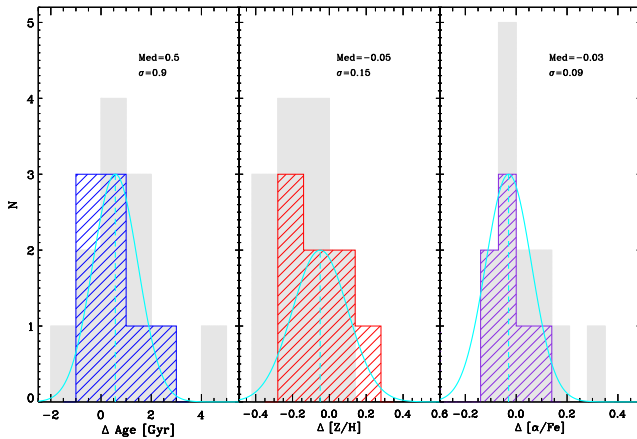


Figure 11. Distribution of the gradients of age (left-hand panel), metallicity (central panel) and α/Fe enhancement (right-hand panel) for the sample bulges. The dashed line represents the median of the distribution and its values is reported. Solid line represents a Gaussian centred in the median value of distribution. Its σ approximated by the value containing the 68% of the objects of the distribution is reported. In grey is represented the distribution of the same quantities obtained by Morelli et al. (2008) for the bulges of HSB discs.

0.4) are consistent with the correlation found by Morelli et al. (2008) and Rawle et al. (2010) for the bulges in HSB galaxies and early-type galaxies, respectively. This is not the case of the few remaining bulges with a very low central metallicity value ($-1.1 < [Z/H] < -0.5$). If confirmed with more firm statistics, such a result would favor the importance of dissipative collapse in the assembly of bulges (Arimoto & Yoshii 1987; Pipino et al. 2010).

No correlation has been found between the central value and gradient of α/Fe enhancement the right-hand panel of Fig. 12. This is in agreement with the earlier findings for early-type galaxies Reda et al. (2007) and spiral galaxies (Morelli et al. 2008) and it is expected due to the absence of gradients in the α/Fe radial profiles of the sample galaxies.

5 CONCLUSIONS

The properties of the stellar population of the bulges of a sample of 8 spiral galaxies with LSB discs were investigated to constrain the dominant mechanism at the epoch of their assembly.

- The central values of the velocity dispersion σ and Mg_b , Mg_2 , H_β , $\langle \text{Fe} \rangle$, and $[\text{MgFe}]'$ line-strength indices were derived from the available spectra for all the sample galaxies. The correlations between Mg_2 , $\langle \text{Fe} \rangle$, H_β , and σ were found to be consistent (and in the case of Mg_2 remarkably similar) to the relations obtained for early-type galaxies and bulges of HSB galaxies (Idiart et al. 1996; Prugniel et al. 2001; Proctor & Sansom 2002; Ganda et al. 2007; Morelli et al. 2008).

- The mean age, total metallicity, and total α/Fe enhancement of the stellar population in the bulge-dominated region of the sample galaxies were derived by using the stellar population models by Thomas et al. (2003). The studied bulges are characterized by a very young stellar population, with a distribution of ages peaked at the value of 1.5 Gyr. They are characterized by ongoing

star formation, confirming previous studies on a few LSB galaxies (Bergmann et al. 2003). The metallicity of the sample bulges spans a large range of values from high ($[Z/H] = 0.30$ dex) to sub-solar metallicity ($[Z/H] = -1.0$ dex). Most of them display solar α/Fe enhancements. These properties resemble closely the properties of the bulges hosted in HSB galaxies and suggest a formation through a dissipative collapse with a short star-formation time-scale (Thomas et al. 2005). For the galaxies with sub-solar values of the α/Fe enhancement, other mechanism of bulge formation as redistribution of disc material due to the presence of a bar or environmental effects (Kormendy & Kennicutt 2004; Moorthy & Holtzman 2006) need to be considered.

- We do not find any correlation between the age, metallicity, and α/Fe enhancement and morphological type. Although we lack of S0 galaxies because our galaxies ranges from Sa to Sm, we can exclude a strong interplay between the bulge and disc components. There is a correlation between the velocity dispersion, age, metallicity, and α/Fe enhancement. In agreement with the bulges of the LSB discs the most massive bulges of our sample galaxies, more metal rich, and characterized by a shorter star-formation time-scale.

- The bulge of the barred galaxy ESO-LV 4880490 has an intermediate age (3 Gyr), low metallicity, ($[Z/H] = -1.07$ dex) and sub-solar α/Fe ratio ($[\alpha/\text{Fe}] = -0.24$ dex). These properties are consistent with a slow buildup within a scenario of secular evolution driven by the bar.

- Most of the sample galaxies show no gradient in age and $[\alpha/\text{Fe}]$ radial profiles. This is in agreement with the earlier findings by Jablonka et al. (2007); Morelli et al. (2008) for the bulges of HSB galaxies. The presence of negative gradient in the metallicity radial profile in some of the sample bulges suggest a formation via dissipative collapse (Eggen et al. 1962; Larson 1974). In this framework, a strong interplay between the star-formation time-scale and gas flows is needed to explain the coexistence of the metallicity gradient with the absence of α/Fe gradient (Pipino et al. 2008), as observed in our data. However, in most of our bulges no metallicity gradient is measured. This suggests that a pure dissipative collapse is not able to explain formation of the bulges of all the LSB galaxies and that other phenomena, like mergers or acquisition events, need to be invoked (Bekki & Shioya 1999; Kobayashi & Arimoto 1999). This picture is also supported by lack of correlation between the central value and gradient of metallicity in bulges with very low metallicity.

In this work, we highlighted that the bulges hosted by LSB galaxies share many structural and chemical properties with the bulges of HSB galaxies. Such a similarity suggests that they possibly had common formation scenarios and evolution histories. Our findings are in agreement with and extend previous results inferred by McGaugh et al. (1995) and Beijersbergen et al. (1999), who compared the photometric properties of the bulges of LSB and HSB galaxies, and Coccato et al. (2008) who performed a detailed analysis of the kinematical and mass-distribution properties of the bulge of the LSB galaxy ESO 323-G064. The fact that bulges hosted in galaxies with very different discs are remarkably similar rules out a relevant interplay between the bulge and disc components and give further support to earlier findings (Thomas & Davies 2006; Morelli et al. 2008). To be definitely confirmed, this prediction requires the detailed comparison between the properties of the stellar populations of both bulges and discs in LSB galaxies.

ACKNOWLEDGMENTS

This work was supported by Padua University through the grants CPDA089220/08, 60A02-5934/09, and 60A02-1283/10 and by Italian Space Agency through the grant ASI-INAF I/009/10/0. L.M. acknowledges financial support from Padua University grant CPS0204. JMA is partially funded by the Spanish MICINN under the Consolider-Ingenio 2010 Program grant CSD2006-00070 and by the Spanish MICINN (grants AYA2007-67965-C03-01 and AYA2010-21887-C04-04). M.C acknowledges financial support from Padua University grants CPDR095001/09 and CPDR115539/11. L.C. has received funding from the European Community's Seventh Framework Programme (FP7/2007-2013) under grant agreement No 229517.

REFERENCES

- Abazajian K. N., Adelman-McCarthy J. K., Agüeros M. A., Allam S. S., Allende Prieto C., An D., Anderson K. S. J., Anderson S. F., Annis J., Bahcall N. A., et al. 2009, *ApJS*, 182, 543
- Aguerri J. A. L., Méndez-Abreu J., Corsini E. M., 2009, *A&A*, 495, 491
- Annibali F., Bressan A., Rampazzo R., Zeilinger W. W., Danese L., 2007, *A&A*, 463, 455
- Arimoto N., Yoshii Y., 1987, *A&A*, 173, 23
- Athanassoula E., 1990, *Annals of the New York Academy of Sciences*, 596, 181
- Beijersbergen M., de Blok W. J. G., van der Hulst J. M., 1999, *A&A*, 351, 903
- Bekki K., Shioya Y., 1999, *ApJ*, 513, 108
- Bergmann M. P., Jørgensen I., Hill G. J., 2003, *AJ*, 125, 116
- Bernardi M., Renzini A., da Costa L. N., Wegner G., Alonso M. V., Pellegrini P. S., Rit e C., Willmer C. N. A., 1998, *ApJL*, 508, L143
- Bettoni D., Galletta G., 1997, *A&AS*, 124, 61
- Bothun G., Impey C., McGaugh S., 1997, *PASP*, 109, 745
- Cappellari M., Emsellem E., 2004, *PASP*, 116, 138
- Cescutti G., Matteucci F., 2011, *A&A*, 525, A126
- Chonis T. S., Gaskell C. M., 2008, *AJ*, 135, 264
- Coccatto L., Swaters R. A., Rubin V. C., D'Odorico S., McGaugh S. S., 2008, *A&A*, 490, 589
- de Lorenzo-C aceres A., Vazdekis A., Aguerri J. A. L., Corsini E. M., Debattista V. P., 2012, *MNRAS*, 420, 1092
- De Lucia G., Kauffmann G., White S. D. M., 2004, *MNRAS*, 349, 1101
- Denicol  G., Terlevich R., Terlevich E., Forbes D. A., Terlevich A., 2005, *MNRAS*, 358, 813
- Eggen O. J., Lynden-Bell D., Sandage A. R., 1962, *ApJ*, 136, 748
- Elmegreen B. G., Bournaud F., Elmegreen D. M., 2008, *ApJ*, 688, 67
- Faber S. M., Friel E. D., Burstein D., Gaskell C. M., 1985, *ApJS*, 57, 711
- Ferreras I., Silk J., 2002, *MNRAS*, 336, 1181
- Ferrers N. M., , 1877, *Quart. J. Pure and Appl. Math.*, 14, 1
- Fisher D., Franx M., Illingworth G., 1996, *ApJ*, 459, 110
- Galaz G., Dalcanton J. J., Infante L., Treister E., 2002, *AJ*, 124, 1360
- Galaz G., Herrera-Camus R., Garcia-Lambas D., Padilla N., 2011, *ApJ*, 728, 74
- Galaz G., Villalobos A., Infante L., Donzelli C., 2006, *AJ*, 131, 2035
- Ganda K., Peletier R. F., McDermid R. M., Falc n-Barroso J., de Zeeuw P. T., Bacon R., Cappellari M., Davies R. L., Emsellem E., Krajnovi  D., Kuntschner H., Sarzi M., van de Ven G., 2007, *MNRAS*, 380, 506
- Gerhard O. E., 1993, *MNRAS*, 265, 213
- Gilmore G., Wyse R. F. G., 1998, *AJ*, 116, 748
- Gorgas J., Efstathiou G., Salamanca A. A., 1990, *MNRAS*, 245, 217
- Hopkins P. F., Cox T. J., Dutta S. N., Hernquist L., Kormendy J., Lauer T. R., 2009, *ApJS*, 181, 135
- Idiart T. P., de Freitas Pacheco J. A., Costa R. D. D., 1996, *AJ*, 112, 2541
- Impey C., Burkholder V., Sprayberry D., 2001, *AJ*, 122, 2341
- Impey C. D., Sprayberry D., Irwin M. J., Bothun G. D., 1996, *ApJS*, 105, 209
- Jablonka P., Gorgas J., Goudfrooij P., 2007, *ArXiv e-prints*, 707
- J rgensen I., 1999a, *MNRAS*, 306, 607
- J rgensen I., 1999b, *MNRAS*, 306, 607
- Kawata D., 2001, *ApJ*, 558, 598
- Kawata D., Gibson B. K., 2003, *MNRAS*, 340, 908
- Kobayashi C., 2004, *MNRAS*, 347, 740
- Kobayashi C., Arimoto N., 1999, *ApJ*, 527, 573
- Kodama T., Arimoto N., Barger A. J., Arag' on-Salamanca A., 1998, *A&A*, 334, 99
- Kormendy J., Fisher D. B., Cornell M. E., Bender R., 2009, *ApJS*, 182, 216
- Kormendy J., Kennicutt R. C., 2004, *ARA&A*, 42, 603
- Kuntschner H., 2000, *MNRAS*, 315, 184
- Kuntschner H., Lucey J. R., Smith R. J., Hudson M. J., Davies R. L., 2001, *MNRAS*, 323, 615
- Larson R. B., 1974, *MNRAS*, 166, 585
- Laurikainen E., Salo H., Buta R., 2005, *MNRAS*, 362, 1319
- Liang Y. C., Zhong G. H., Hammer F., Chen X. Y., Liu F. S., Gao D., Hu J. Y., Deng L. C., Zhang B., 2010, *MNRAS*, 409, 213
- MacArthur L. A., Gonz lez J. J., Courteau S., 2009, *MNRAS*, 395, 28
- Markwardt C. B., 2009, in D. A. Bohlender, D. Durand, & P. Dowler ed., *Astronomical Data Analysis Software and Systems XVIII* Vol. 411 of *Astronomical Society of the Pacific Conference Series*, Non-linear Least-squares Fitting in IDL with MPFIT. p. 251
- Matteucci F., 1994, *A&A*, 288, 57
- McGaugh S. S., Schombert J. M., Bothun G. D., 1995, *AJ*, 109, 2019
- Mehlert D., Saglia R. P., Bender R., Wegner G., 1998, *A&A*, 332, 33
- Mehlert D., Thomas D., Saglia R. P., Bender R., Wegner G., 2003, *A&A*, 407, 423
- M ndez-Abreu J., Aguerri J. A. L., Corsini E. M., Simonneau E., 2008, *A&A*, 478, 353
- Moorthy B. K., Holtzman J. A., 2006, *MNRAS*, 371, 583
- Mor  J. J., Garbow B. S., Hillstrom K. E., 1980, *Argonne National Laboratory Report ANL-80-74*
- Morelli L., Halliday C., Corsini E. M., Pizzella A., Thomas D., Saglia R. P., Davies R. L., Bender R., Birkinshaw M., Bertola F., 2004, *MNRAS*, 354, 753
- Morelli L., Pompei E., Pizzella A., M ndez-Abreu J., Corsini E. M., Coccatto L., Saglia R. P., Sarzi M., Bertola F., 2008, *MNRAS*, 389, 341
- Nelan J. E., Smith R. J., Hudson M. J., Wegner G. A., Lucey J. R., Moore S. A. W., Quinney S. J., Suntzeff N. B., 2005, *ApJ*, 632, 137

- Peletier R. F., 1989, PhD thesis, University of Groningen
- Pipino A., D'Ercole A., Chiappini C., Matteucci F., 2010, *MNRAS*, 407, 1347
- Pipino A., D'Ercole A., Matteucci F., 2008, *A&A*, 484, 679
- Pizzella A., Corsini E. M., Sarzi M., Magorrian J., Méndez-Abreu J., Coccato L., Morelli L., Bertola F., 2008, *MNRAS*, 387, 1099
- Proctor R. N., Sansom A. E., 2002, *MNRAS*, 333, 517
- Prugniel P., Maubon G., Simien F., 2001, *A&A*, 366, 68
- Prugniel P., Soubiran C., 2001, *A&A*, 369, 1048
- Rampazzo R., Annibali F., Bressan A., Longhetti M., Padoan F., Zeilinger W. W., 2005, *A&A*, 433, 497
- Ramya S., Prabhu T. P., Das M., 2011, *MNRAS*, 418, 789
- Rawle T. D., Smith R. J., Lucey J. R., 2010, *MNRAS*, 401, 852
- Reda F. M., Proctor R. N., Forbes D. A., Hau G. K. T., Larsen S. S., 2007, *MNRAS*, 377, 1772
- Sánchez-Blázquez P., Gorgas J., Cardiel N., 2006, *A&A*, 457, 823
- Sánchez-Blázquez P., Gorgas J., Cardiel N., González J. J., 2006, *A&A*, 457, 809
- Sánchez-Blázquez P., Ocvirk P., Gibson B. K., Pérez I., Peletier R. F., 2011, *MNRAS*, 415, 709
- Sarzi M., Falcón-Barroso J., Davies R. L., Bacon R., Bureau M., Cappellari M., de Zeeuw P. T., Emsellem E., Fathi K., Krajnović D., Kuntschner H., McDermid R. M., Peletier R. F., 2006, *MNRAS*, 366, 1151
- Spolaor M., Kobayashi C., Forbes D. A., Couch W. J., Hau G. K. T., 2010, *MNRAS*, 408, 272
- Tassis K., Kravtsov A. V., Gnedin N. Y., 2008, *ApJ*, 672, 888
- Thomas D., Davies R. L., 2006, *MNRAS*, 366, 510
- Thomas D., Maraston C., Bender R., 2003, *MNRAS*, 339, 897
- Thomas D., Maraston C., Bender R., Mendes de Oliveira C., 2005, *ApJ*, 621, 673
- Trager S. C., Faber S. M., Worthey G., González J. J., 2000, *AJ*, 119, 1645
- Trager S. C., Worthey G., Faber S. M., Burstein D., Gonzalez J. J., 1998, *ApJS*, 116, 1
- van der Hulst J. M., Skillman E. D., Smith T. R., Bothun G. D., McGaugh S. S., de Blok W. J. G., 1993, *AJ*, 106, 548
- van der Marel R. P., Franx M., 1993, *ApJ*, 407, 525
- Vorobyov E. I., Shchekinov Y., Bizyaev D., Bomans D., Dettmar R.-J., 2009, *A&A*, 505, 483
- Worthey G., Faber S. M., Gonzalez J. J., Burstein D., 1994, *ApJS*, 94, 687
- Worthey G., Ottaviani D. L., 1997, *ApJS*, 111, 377
- Wozniak H., Pfenniger D., 1997, *A&A*, 317, 14
- Zackrisson E., Bergvall N., Östlin G., 2005, *A&A*, 435, 29
- Zhao Y., 2012, *Astrophysics and Space Science*, 337, 719
- Zhong G. H., Liang Y. C., Hammer F., Chen X. Y., Deng L. C., Flores H., 2010, *A&A*, 520, A69

APPENDIX A: STELLAR KINEMATICS AND LINE STRENGTH INDICES.

The stellar kinematics of PGC 26148 and PGC 37759 and the line-strength indices for all the sample galaxies are given in Table A1 and A2 respectively. The stellar kinematics of the remaining sample galaxies is given in Paper I.

This paper has been typeset from a \TeX / \LaTeX file prepared by the author.

Table A1. Stellar kinematics of the sample galaxies.

r [arcsec] (1)	v (\AA) (2)	σ (mag) (3)	h_3 (\AA) (4)	h_4 (\AA) (5)
PGC 26148 - MJ				
-7.43	-3.1 ± 2.4	42.8 ± 2.7	-0.004 ± 0.036	0.026 ± 0.041
-4.70	14.5 ± 2.4	70.9 ± 1.9	-0.069 ± 0.018	-0.006 ± 0.022
-2.40	13.2 ± 2.6	94.7 ± 2.2	-0.042 ± 0.016	-0.014 ± 0.018
-1.19	0.1 ± 2.0	103.8 ± 2.4	0.010 ± 0.015	0.016 ± 0.015
-0.75	-6.2 ± 2.6	84.8 ± 2.6	0.021 ± 0.016	0.093 ± 0.019
-0.50	-6.9 ± 2.0	83.6 ± 2.1	0.014 ± 0.014	0.081 ± 0.016
-0.25	-6.5 ± 1.6	88.1 ± 1.6	-0.022 ± 0.011	0.043 ± 0.012
0.07	-0.6 ± 1.7	92.1 ± 1.6	-0.028 ± 0.012	0.003 ± 0.013
0.25	-0.4 ± 1.7	89.0 ± 1.6	-0.027 ± 0.012	-0.009 ± 0.013
0.50	12.2 ± 1.7	84.4 ± 2.2	-0.051 ± 0.015	0.060 ± 0.017
0.85	3.6 ± 2.0	96.0 ± 2.6	-0.036 ± 0.015	0.077 ± 0.017
1.65	-3.2 ± 2.1	103.8 ± 2.2	-0.049 ± 0.015	-0.007 ± 0.016
3.63	-15.0 ± 1.7	75.5 ± 1.7	0.017 ± 0.017	-0.044 ± 0.019
6.69	-1.3 ± 3.5	40.5 ± 3.1	0.034 ± 0.036	0.010 ± 0.050
PGC 37759 - MJ				
-11.13	139.2 ± 4.1	31.0 ± 6.3	-0.002 ± 0.069	0.019 ± 0.125
-7.89	139.4 ± 2.9	44.1 ± 4.5	0.051 ± 0.051	0.036 ± 0.071
-6.13	128.6 ± 3.0	31.5 ± 4.3	-0.037 ± 0.078	0.050 ± 0.081
-4.62	120.2 ± 2.4	40.2 ± 2.8	-0.045 ± 0.053	-0.053 ± 0.049
-3.23	94.9 ± 3.0	41.0 ± 3.8	0.024 ± 0.056	0.039 ± 0.058
-2.13	72.4 ± 3.2	64.5 ± 4.3	-0.110 ± 0.035	0.153 ± 0.043
-1.22	42.9 ± 2.8	61.2 ± 3.6	-0.093 ± 0.030	0.104 ± 0.039
-0.61	33.6 ± 2.7	64.9 ± 3.5	-0.061 ± 0.029	0.089 ± 0.035
-0.25	11.5 ± 3.2	62.1 ± 3.5	-0.066 ± 0.032	0.036 ± 0.040
0.00	3.9 ± 3.0	65.4 ± 3.2	-0.015 ± 0.028	0.071 ± 0.032
0.25	-10.3 ± 2.5	62.6 ± 2.8	-0.021 ± 0.028	0.015 ± 0.034
0.50	-22.5 ± 2.8	63.7 ± 2.3	0.004 ± 0.029	-0.040 ± 0.029
0.86	-39.2 ± 2.7	66.3 ± 3.0	-0.003 ± 0.030	0.019 ± 0.031
1.47	-47.5 ± 2.6	60.0 ± 2.9	-0.029 ± 0.029	0.019 ± 0.038
2.37	-79.7 ± 2.7	56.2 ± 3.5	0.064 ± 0.035	0.028 ± 0.044
3.37	-102.3 ± 2.6	42.8 ± 3.7	0.065 ± 0.041	0.042 ± 0.063
4.57	-108.6 ± 2.3	40.8 ± 3.7	-0.061 ± 0.041	0.023 ± 0.066
6.41	-119.1 ± 2.6	40.7 ± 3.5	-0.008 ± 0.054	0.044 ± 0.052
8.07	-123.8 ± 3.4	31.6 ± 4.1	-0.022 ± 0.090	0.051 ± 0.071
10.30	-133.2 ± 3.8	32.7 ± 4.2	-0.010 ± 0.095	0.045 ± 0.060
PGC 37759 - MN				
-12.36	-19.8 ± 9.5	32.0 ± 14.0	-0.026 ± 0.221	-0.019 ± 0.252
-2.11	-2.9 ± 2.9	44.2 ± 4.5	-0.034 ± 0.044	0.008 ± 0.077
-0.54	-6.9 ± 3.0	66.4 ± 2.7	0.033 ± 0.037	-0.083 ± 0.035
0.05	16.3 ± 2.3	60.7 ± 3.3	-0.061 ± 0.030	0.062 ± 0.037
0.53	25.7 ± 2.8	65.2 ± 3.6	0.035 ± 0.034	0.026 ± 0.038
1.80	2.6 ± 3.0	52.7 ± 4.1	-0.040 ± 0.044	0.048 ± 0.053
10.48	-14.9 ± 11.8	44.0 ± 18.9	0.036 ± 0.158	-0.018 ± 0.296

Table A2. Line-strength indices of the sample galaxies.

r [arcsec] (1)	H β (Å) (2)	Mg 2 (mag) (3)	Mg b (Å) (4)	Fe5270 (Å) (5)	Fe5335 (Å) (6)
ESO-LV 1860550 - MJ+30°					
-10.88	3.347 ± 0.134	0.131 ± 0.004	2.501 ± 0.126	2.164 ± 0.149	1.707 ± 0.139
-7.70	2.666 ± 0.116	0.153 ± 0.003	2.843 ± 0.108	2.399 ± 0.127	1.889 ± 0.117
-5.58	2.275 ± 0.105	0.177 ± 0.003	3.100 ± 0.100	2.310 ± 0.118	1.958 ± 0.109
-4.09	2.092 ± 0.093	0.185 ± 0.003	3.175 ± 0.087	2.661 ± 0.101	2.253 ± 0.094
-2.97	2.168 ± 0.099	0.191 ± 0.003	3.440 ± 0.091	2.461 ± 0.106	2.124 ± 0.098
-2.10	2.100 ± 0.086	0.196 ± 0.002	3.323 ± 0.074	2.650 ± 0.086	2.265 ± 0.078
-1.49	2.055 ± 0.114	0.202 ± 0.003	3.341 ± 0.102	2.636 ± 0.113	2.146 ± 0.102
-0.99	1.594 ± 0.112	0.201 ± 0.003	3.418 ± 0.106	2.633 ± 0.107	2.364 ± 0.100
-0.49	1.925 ± 0.095	0.206 ± 0.003	3.413 ± 0.088	2.776 ± 0.086	2.361 ± 0.080
-0.12	2.046 ± 0.087	0.209 ± 0.002	3.510 ± 0.083	2.596 ± 0.082	2.398 ± 0.078
0.13	2.117 ± 0.079	0.210 ± 0.002	3.473 ± 0.076	2.757 ± 0.076	2.327 ± 0.074
0.50	1.977 ± 0.089	0.207 ± 0.003	3.335 ± 0.089	2.720 ± 0.089	2.460 ± 0.086
1.00	1.979 ± 0.102	0.206 ± 0.003	3.391 ± 0.112	2.564 ± 0.107	2.296 ± 0.108
1.50	2.049 ± 0.117	0.208 ± 0.004	3.351 ± 0.128	2.450 ± 0.124	2.201 ± 0.124
2.11	2.039 ± 0.113	0.204 ± 0.004	3.317 ± 0.126	2.605 ± 0.127	2.121 ± 0.123
2.97	2.109 ± 0.121	0.197 ± 0.004	3.284 ± 0.131	2.634 ± 0.130	2.166 ± 0.125
4.22	2.317 ± 0.106	0.187 ± 0.003	3.263 ± 0.111	2.499 ± 0.109	2.318 ± 0.103
5.97	2.600 ± 0.112	0.161 ± 0.003	2.749 ± 0.115	2.605 ± 0.110	2.038 ± 0.107
8.29	2.960 ± 0.148	0.145 ± 0.005	2.657 ± 0.151	2.053 ± 0.144	1.707 ± 0.143
13.65	2.455 ± 0.171	0.092 ± 0.005	1.543 ± 0.175	1.372 ± 0.166	1.464 ± 0.170
ESO-LV 1860550 - MN+30°					
-8.01	3.133 ± 0.220	0.113 ± 0.007	2.381 ± 0.177	1.903 ± 0.181	1.553 ± 0.206
-5.59	2.897 ± 0.187	0.149 ± 0.006	2.666 ± 0.145	2.026 ± 0.147	2.343 ± 0.164
-4.27	2.541 ± 0.165	0.168 ± 0.005	2.824 ± 0.128	1.936 ± 0.129	2.027 ± 0.137
-3.42	2.436 ± 0.137	0.170 ± 0.004	3.049 ± 0.117	2.425 ± 0.112	2.138 ± 0.117
-2.80	2.424 ± 0.158	0.191 ± 0.005	2.994 ± 0.135	2.510 ± 0.126	2.299 ± 0.131
-2.30	2.011 ± 0.139	0.190 ± 0.004	3.343 ± 0.115	2.367 ± 0.111	2.313 ± 0.114
-1.80	2.005 ± 0.131	0.194 ± 0.004	3.307 ± 0.108	2.450 ± 0.103	2.200 ± 0.105
-1.43	2.085 ± 0.156	0.198 ± 0.005	3.129 ± 0.125	2.552 ± 0.121	2.378 ± 0.119
-1.18	2.340 ± 0.144	0.206 ± 0.004	3.518 ± 0.111	2.626 ± 0.112	2.637 ± 0.110
-0.93	2.168 ± 0.132	0.203 ± 0.004	3.411 ± 0.103	2.431 ± 0.105	2.284 ± 0.101
-0.68	1.705 ± 0.122	0.202 ± 0.004	3.454 ± 0.098	2.676 ± 0.100	2.227 ± 0.096
-0.43	2.188 ± 0.119	0.210 ± 0.004	3.483 ± 0.097	2.643 ± 0.099	2.421 ± 0.094
-0.18	2.076 ± 0.108	0.212 ± 0.003	3.394 ± 0.089	2.887 ± 0.090	2.730 ± 0.085
0.07	2.092 ± 0.097	0.206 ± 0.003	3.365 ± 0.085	2.902 ± 0.084	2.583 ± 0.078
0.32	1.931 ± 0.102	0.206 ± 0.003	3.401 ± 0.097	2.592 ± 0.094	2.382 ± 0.089
0.57	1.919 ± 0.112	0.207 ± 0.004	3.223 ± 0.110	2.544 ± 0.108	2.330 ± 0.102
0.82	1.843 ± 0.124	0.203 ± 0.004	3.342 ± 0.123	2.524 ± 0.121	2.320 ± 0.115
1.07	1.719 ± 0.137	0.206 ± 0.005	3.448 ± 0.139	2.527 ± 0.135	2.177 ± 0.129
1.32	1.695 ± 0.151	0.205 ± 0.005	3.530 ± 0.154	2.606 ± 0.149	2.637 ± 0.143
1.57	1.556 ± 0.154	0.200 ± 0.005	3.326 ± 0.159	2.560 ± 0.153	2.811 ± 0.145
1.93	2.051 ± 0.137	0.204 ± 0.005	3.208 ± 0.143	2.793 ± 0.143	3.206 ± 0.137
2.43	1.966 ± 0.144	0.197 ± 0.005	3.274 ± 0.149	2.370 ± 0.144	2.116 ± 0.143
2.94	1.987 ± 0.157	0.194 ± 0.005	3.449 ± 0.157	2.574 ± 0.148	2.167 ± 0.149
3.56	2.322 ± 0.145	0.184 ± 0.005	3.065 ± 0.145	2.640 ± 0.136	2.409 ± 0.138
4.31	2.702 ± 0.154	0.171 ± 0.005	3.075 ± 0.152	2.160 ± 0.144	2.244 ± 0.144
5.16	3.002 ± 0.178	0.171 ± 0.006	2.867 ± 0.174	2.206 ± 0.166	1.709 ± 0.167
6.47	2.760 ± 0.181	0.150 ± 0.006	2.849 ± 0.181	1.916 ± 0.176	1.808 ± 0.175
9.15	3.311 ± 0.239	0.134 ± 0.008	2.308 ± 0.225	1.284 ± 0.230	1.413 ± 0.231
ESO-LV 2060140 - MJ					
-37.52	3.153 ± 0.307	0.085 ± 0.008	1.290 ± 0.263	1.433 ± 0.362	0.217 ± 0.251
-26.68	3.644 ± 0.402	0.070 ± 0.011	1.661 ± 0.342	1.105 ± 0.438	1.405 ± 0.299
-20.38	3.791 ± 0.372	0.066 ± 0.011	1.728 ± 0.335	1.199 ± 0.456	1.197 ± 0.297

Table A2 – *continued*

(1)	(2)	(3)	(4)	(5)	(6)
-13.98	3.464 ± 0.331	0.081 ± 0.010	1.977 ± 0.296	1.776 ± 0.426	1.407 ± 0.286
-10.08	3.346 ± 0.215	0.093 ± 0.007	1.959 ± 0.193	1.689 ± 0.282	1.358 ± 0.195
-7.45	3.189 ± 0.188	0.106 ± 0.006	2.151 ± 0.172	1.808 ± 0.248	1.676 ± 0.172
-5.20	3.096 ± 0.172	0.100 ± 0.005	1.934 ± 0.158	1.747 ± 0.231	1.768 ± 0.158
-3.45	2.882 ± 0.169	0.106 ± 0.005	1.971 ± 0.155	2.066 ± 0.224	1.941 ± 0.153
-2.20	2.928 ± 0.134	0.112 ± 0.005	2.089 ± 0.131	1.997 ± 0.192	1.920 ± 0.131
-1.34	3.513 ± 0.128	0.117 ± 0.004	2.005 ± 0.133	2.085 ± 0.196	1.652 ± 0.131
-0.72	3.509 ± 0.100	0.100 ± 0.003	2.140 ± 0.103	2.107 ± 0.156	1.853 ± 0.107
-0.23	3.401 ± 0.132	0.093 ± 0.004	2.024 ± 0.122	1.972 ± 0.180	1.594 ± 0.121
0.25	3.275 ± 0.148	0.127 ± 0.004	2.032 ± 0.129	2.019 ± 0.181	1.813 ± 0.120
0.86	2.793 ± 0.185	0.145 ± 0.006	2.446 ± 0.168	2.274 ± 0.236	1.766 ± 0.157
1.74	2.880 ± 0.163	0.128 ± 0.005	2.216 ± 0.156	1.872 ± 0.223	1.655 ± 0.152
2.98	3.099 ± 0.151	0.116 ± 0.005	2.170 ± 0.149	2.289 ± 0.217	1.810 ± 0.152
4.62	3.044 ± 0.160	0.108 ± 0.006	2.165 ± 0.161	2.320 ± 0.235	1.543 ± 0.162
6.62	3.319 ± 0.174	0.108 ± 0.006	2.146 ± 0.176	1.786 ± 0.258	1.450 ± 0.182
8.88	3.432 ± 0.164	0.091 ± 0.006	1.795 ± 0.157	1.644 ± 0.250	1.459 ± 0.183
11.92	3.484 ± 0.214	0.095 ± 0.008	1.873 ± 0.205	2.013 ± 0.313	1.610 ± 0.231
17.02	3.775 ± 0.201	0.071 ± 0.008	1.705 ± 0.205	2.037 ± 0.313	1.507 ± 0.241
23.65	3.732 ± 0.286	0.058 ± 0.010	2.011 ± 0.255	1.658 ± 0.416	0.757 ± 0.322
ESO-LV 2060140 - MN					
-12.50	3.188 ± 0.361	0.072 ± 0.010	1.761 ± 0.251	2.129 ± 0.368	1.752 ± 0.332
-7.25	3.251 ± 0.326	0.093 ± 0.010	1.641 ± 0.243	1.845 ± 0.348	1.669 ± 0.304
-4.30	2.870 ± 0.308	0.104 ± 0.009	1.523 ± 0.227	1.579 ± 0.326	1.820 ± 0.282
-2.70	2.818 ± 0.273	0.117 ± 0.008	2.569 ± 0.228	1.704 ± 0.303	1.504 ± 0.254
-1.70	3.366 ± 0.264	0.126 ± 0.008	2.570 ± 0.221	1.664 ± 0.305	1.595 ± 0.262
-1.08	4.300 ± 0.290	0.118 ± 0.009	2.169 ± 0.244	2.246 ± 0.345	1.409 ± 0.299
-0.72	4.811 ± 0.393	0.108 ± 0.012	2.389 ± 0.346	1.711 ± 0.470	1.866 ± 0.407
-0.47	4.134 ± 0.327	0.087 ± 0.010	1.952 ± 0.283	1.092 ± 0.389	1.165 ± 0.337
-0.22	3.778 ± 0.386	0.074 ± 0.010	1.610 ± 0.305	1.854 ± 0.377	1.760 ± 0.327
0.03	2.872 ± 0.331	0.121 ± 0.008	1.367 ± 0.241	1.962 ± 0.274	1.795 ± 0.233
0.28	4.009 ± 0.346	0.158 ± 0.008	1.864 ± 0.250	2.580 ± 0.272	0.955 ± 0.227
0.64	3.416 ± 0.313	0.149 ± 0.008	1.490 ± 0.240	2.095 ± 0.264	1.550 ± 0.211
1.14	2.809 ± 0.329	0.145 ± 0.008	1.985 ± 0.268	1.944 ± 0.294	2.018 ± 0.242
1.88	2.578 ± 0.296	0.136 ± 0.008	1.771 ± 0.261	3.157 ± 0.293	1.280 ± 0.234
3.11	2.703 ± 0.314	0.122 ± 0.009	1.845 ± 0.276	2.154 ± 0.331	1.386 ± 0.257
5.17	2.774 ± 0.305	0.112 ± 0.009	1.544 ± 0.277	1.953 ± 0.336	1.437 ± 0.264
9.24	3.356 ± 0.280	0.111 ± 0.009	1.950 ± 0.267	1.650 ± 0.333	2.253 ± 0.266
13.81	3.928 ± 0.352	0.108 ± 0.010	1.281 ± 0.331	2.100 ± 0.377	2.431 ± 0.296
ESO-LV 2340130 - MJ+16°					
-22.03	4.012 ± 0.258	0.054 ± 0.007	1.321 ± 0.274	0.552 ± 0.270	0.876 ± 0.220
-12.62	3.592 ± 0.152	0.089 ± 0.004	2.050 ± 0.158	1.483 ± 0.150	1.254 ± 0.126
-8.99	3.651 ± 0.124	0.108 ± 0.003	2.112 ± 0.129	1.795 ± 0.119	1.545 ± 0.100
-6.66	3.630 ± 0.149	0.098 ± 0.003	1.737 ± 0.127	1.556 ± 0.120	1.337 ± 0.101
-5.10	3.735 ± 0.168	0.091 ± 0.003	1.487 ± 0.143	1.468 ± 0.134	1.255 ± 0.113
-3.71	3.779 ± 0.121	0.108 ± 0.003	2.165 ± 0.114	1.467 ± 0.104	1.433 ± 0.085
-2.58	3.497 ± 0.124	0.113 ± 0.003	1.838 ± 0.113	1.762 ± 0.102	1.464 ± 0.083
-1.71	3.471 ± 0.117	0.115 ± 0.002	2.370 ± 0.107	1.828 ± 0.098	1.644 ± 0.078
-1.09	3.875 ± 0.145	0.103 ± 0.003	1.572 ± 0.126	1.490 ± 0.114	1.535 ± 0.092
-0.59	4.239 ± 0.130	0.090 ± 0.003	1.346 ± 0.111	1.440 ± 0.108	1.215 ± 0.081
-0.23	4.325 ± 0.109	0.085 ± 0.002	1.227 ± 0.095	1.294 ± 0.093	1.242 ± 0.068
0.02	4.155 ± 0.102	0.080 ± 0.002	1.147 ± 0.091	1.326 ± 0.091	1.143 ± 0.066
0.27	4.036 ± 0.149	0.084 ± 0.003	1.702 ± 0.138	1.091 ± 0.139	1.150 ± 0.104
0.63	3.939 ± 0.235	0.092 ± 0.005	1.678 ± 0.229	1.360 ± 0.251	1.154 ± 0.175
1.13	3.501 ± 0.278	0.104 ± 0.007	1.928 ± 0.285	1.347 ± 0.302	1.185 ± 0.219
1.75	3.599 ± 0.204	0.118 ± 0.005	2.197 ± 0.202	1.744 ± 0.213	1.666 ± 0.151
2.63	3.462 ± 0.160	0.108 ± 0.004	2.193 ± 0.160	1.677 ± 0.167	1.592 ± 0.111
3.78	3.958 ± 0.122	0.104 ± 0.003	2.058 ± 0.122	1.556 ± 0.128	1.489 ± 0.085
5.00	4.082 ± 0.150	0.099 ± 0.004	2.035 ± 0.142	1.157 ± 0.149	1.381 ± 0.103

Table A2 – continued

(1)	(2)	(3)	(4)	(5)	(6)
6.35	3.676 ± 0.167	0.101 ± 0.004	1.962 ± 0.171	1.735 ± 0.186	1.461 ± 0.118
8.31	3.606 ± 0.161	0.109 ± 0.004	2.205 ± 0.171	1.709 ± 0.192	1.669 ± 0.126
11.17	3.686 ± 0.136	0.092 ± 0.004	1.884 ± 0.150	1.564 ± 0.173	1.498 ± 0.117
16.35	3.601 ± 0.204	0.085 ± 0.006	1.677 ± 0.223	0.910 ± 0.254	1.375 ± 0.176
ESO-LV 2340130 - MN+16°					
-7.35	3.677 ± 0.155	0.077 ± 0.004	2.092 ± 0.133	1.399 ± 0.157	1.226 ± 0.144
-3.90	3.621 ± 0.129	0.096 ± 0.003	1.777 ± 0.103	1.597 ± 0.120	1.377 ± 0.111
-2.51	3.620 ± 0.136	0.082 ± 0.003	1.253 ± 0.091	1.412 ± 0.106	1.296 ± 0.100
-1.67	3.172 ± 0.165	0.099 ± 0.004	1.851 ± 0.115	1.560 ± 0.134	1.599 ± 0.116
-1.04	3.503 ± 0.138	0.102 ± 0.003	1.779 ± 0.097	1.662 ± 0.112	1.549 ± 0.097
-0.54	3.638 ± 0.137	0.088 ± 0.003	1.379 ± 0.088	1.474 ± 0.110	1.235 ± 0.091
-0.18	4.129 ± 0.127	0.080 ± 0.003	1.278 ± 0.089	1.234 ± 0.110	1.159 ± 0.090
0.07	3.952 ± 0.112	0.080 ± 0.003	1.202 ± 0.087	1.130 ± 0.107	0.902 ± 0.089
0.32	3.939 ± 0.152	0.088 ± 0.004	1.639 ± 0.130	1.233 ± 0.160	1.073 ± 0.142
0.68	3.755 ± 0.198	0.095 ± 0.006	1.785 ± 0.177	1.089 ± 0.227	1.270 ± 0.202
1.29	3.133 ± 0.214	0.102 ± 0.006	1.757 ± 0.180	1.400 ± 0.230	1.388 ± 0.203
2.18	2.984 ± 0.150	0.103 ± 0.004	2.051 ± 0.120	1.652 ± 0.147	1.477 ± 0.133
3.29	3.992 ± 0.131	0.101 ± 0.004	2.084 ± 0.108	1.798 ± 0.135	1.569 ± 0.123
5.15	3.442 ± 0.178	0.111 ± 0.005	2.069 ± 0.157	1.734 ± 0.195	1.397 ± 0.183
ESO-LV 4000370 - MJ+44°					
-23.69	3.234 ± 0.380	0.016 ± 0.011	1.129 ± 0.456	1.191 ± 0.475	2.462 ± 0.571
-15.54	3.331 ± 0.261	0.042 ± 0.008	0.943 ± 0.332	0.927 ± 0.337	0.846 ± 0.414
-11.78	3.622 ± 0.295	0.033 ± 0.008	1.165 ± 0.331	0.508 ± 0.338	1.496 ± 0.417
-8.78	3.068 ± 0.246	0.080 ± 0.008	2.120 ± 0.297	1.529 ± 0.293	1.339 ± 0.356
-6.99	3.752 ± 0.259	0.054 ± 0.007	1.280 ± 0.284	0.858 ± 0.293	0.867 ± 0.363
-5.89	3.496 ± 0.232	0.057 ± 0.007	1.155 ± 0.254	1.376 ± 0.273	1.485 ± 0.329
-4.89	3.597 ± 0.243	0.071 ± 0.007	0.851 ± 0.264	1.317 ± 0.286	2.241 ± 0.332
-4.01	2.772 ± 0.253	0.083 ± 0.007	1.450 ± 0.276	1.839 ± 0.308	2.024 ± 0.329
-3.28	2.415 ± 0.258	0.097 ± 0.008	1.708 ± 0.275	1.417 ± 0.316	1.551 ± 0.337
-2.51	3.011 ± 0.216	0.077 ± 0.006	1.218 ± 0.231	1.691 ± 0.264	1.761 ± 0.282
-1.89	2.364 ± 0.245	0.093 ± 0.007	1.637 ± 0.260	1.923 ± 0.295	1.938 ± 0.316
-1.39	2.544 ± 0.214	0.087 ± 0.006	1.986 ± 0.228	1.785 ± 0.265	1.558 ± 0.281
-0.89	3.033 ± 0.208	0.087 ± 0.006	2.044 ± 0.222	2.314 ± 0.260	1.858 ± 0.274
-0.39	2.690 ± 0.193	0.094 ± 0.006	1.825 ± 0.213	1.699 ± 0.242	1.396 ± 0.259
0.11	2.896 ± 0.199	0.098 ± 0.006	2.020 ± 0.219	1.443 ± 0.250	1.001 ± 0.264
0.61	2.304 ± 0.204	0.090 ± 0.006	2.490 ± 0.216	1.479 ± 0.248	1.479 ± 0.264
1.11	2.517 ± 0.234	0.087 ± 0.006	1.911 ± 0.240	1.623 ± 0.289	1.675 ± 0.294
1.61	3.066 ± 0.242	0.078 ± 0.006	1.849 ± 0.247	1.423 ± 0.296	1.411 ± 0.289
2.11	3.210 ± 0.236	0.081 ± 0.006	1.810 ± 0.246	1.413 ± 0.292	1.428 ± 0.273
2.73	2.366 ± 0.225	0.081 ± 0.006	1.590 ± 0.236	2.709 ± 0.288	2.053 ± 0.265
3.48	2.951 ± 0.234	0.091 ± 0.006	1.756 ± 0.246	1.527 ± 0.300	1.433 ± 0.278
4.23	3.545 ± 0.230	0.050 ± 0.006	1.034 ± 0.239	1.981 ± 0.294	1.269 ± 0.271
5.10	3.823 ± 0.243	0.031 ± 0.006	0.464 ± 0.243	1.079 ± 0.303	0.764 ± 0.276
6.10	3.851 ± 0.283	0.057 ± 0.007	0.725 ± 0.282	1.295 ± 0.341	1.111 ± 0.315
7.56	2.928 ± 0.259	0.056 ± 0.006	1.427 ± 0.249	1.311 ± 0.307	1.695 ± 0.292
10.08	3.313 ± 0.284	0.058 ± 0.006	1.658 ± 0.264	2.056 ± 0.332	1.220 ± 0.311
12.81	3.618 ± 0.278	0.053 ± 0.006	1.340 ± 0.258	0.942 ± 0.320	1.321 ± 0.299
15.00	3.224 ± 0.281	0.035 ± 0.007	0.480 ± 0.274	0.653 ± 0.352	1.268 ± 0.329
20.59	3.579 ± 0.351	0.052 ± 0.008	1.578 ± 0.329	1.815 ± 0.399	0.949 ± 0.372
ESO-LV 4000370 - MN+44°					
-23.32	3.386 ± 0.523	0.035 ± 0.015	0.646 ± 0.454	0.889 ± 0.457	2.436 ± 0.501
-16.39	4.551 ± 0.413	0.055 ± 0.012	1.152 ± 0.371	0.693 ± 0.377	1.605 ± 0.413
-12.69	3.737 ± 0.409	0.049 ± 0.012	-0.217 ± 0.364	1.145 ± 0.369	0.876 ± 0.401
-10.26	4.678 ± 0.332	0.050 ± 0.010	0.308 ± 0.301	1.841 ± 0.301	1.109 ± 0.331
-8.28	3.485 ± 0.311	0.048 ± 0.009	0.617 ± 0.242	1.396 ± 0.280	1.733 ± 0.298

Table A2 – *continued*

	(1)	(2)	(3)	(4)	(5)	(6)
−6.26	3.135 ± 0.320	0.068 ± 0.009	1.080 ± 0.238	1.374 ± 0.288	1.693 ± 0.296	
−4.50	3.638 ± 0.296	0.085 ± 0.008	1.694 ± 0.216	1.964 ± 0.262	1.518 ± 0.268	
−3.26	2.881 ± 0.288	0.077 ± 0.008	1.878 ± 0.214	1.546 ± 0.258	1.849 ± 0.258	
−2.39	2.719 ± 0.275	0.083 ± 0.008	1.561 ± 0.204	1.581 ± 0.246	1.632 ± 0.245	
−1.77	2.963 ± 0.275	0.084 ± 0.008	1.530 ± 0.207	1.693 ± 0.249	1.647 ± 0.248	
−1.27	2.493 ± 0.252	0.079 ± 0.007	1.508 ± 0.192	2.032 ± 0.227	1.789 ± 0.229	
−0.78	2.354 ± 0.246	0.098 ± 0.007	1.902 ± 0.179	2.109 ± 0.221	1.664 ± 0.222	
−0.28	2.728 ± 0.235	0.095 ± 0.007	1.139 ± 0.173	2.356 ± 0.215	1.555 ± 0.216	
0.22	2.713 ± 0.223	0.085 ± 0.006	1.478 ± 0.170	1.528 ± 0.209	1.400 ± 0.210	
0.72	2.715 ± 0.243	0.078 ± 0.007	1.472 ± 0.192	2.204 ± 0.230	2.098 ± 0.227	
1.22	2.224 ± 0.269	0.094 ± 0.008	1.526 ± 0.198	1.636 ± 0.247	2.317 ± 0.245	
1.84	2.996 ± 0.265	0.079 ± 0.007	1.257 ± 0.195	2.141 ± 0.242	2.305 ± 0.237	
2.59	3.058 ± 0.295	0.083 ± 0.008	1.124 ± 0.213	1.651 ± 0.266	2.605 ± 0.256	
3.46	2.609 ± 0.312	0.070 ± 0.008	1.502 ± 0.232	1.206 ± 0.278	1.676 ± 0.269	
4.71	3.122 ± 0.329	0.072 ± 0.008	1.219 ± 0.237	2.127 ± 0.292	1.004 ± 0.277	
6.33	2.987 ± 0.309	0.077 ± 0.008	2.138 ± 0.208	1.377 ± 0.270	1.028 ± 0.255	
8.09	3.393 ± 0.349	0.056 ± 0.009	1.087 ± 0.232	1.699 ± 0.292	1.751 ± 0.290	
9.96	3.562 ± 0.349	0.061 ± 0.009	1.239 ± 0.235	1.219 ± 0.295	1.354 ± 0.296	
12.27	3.637 ± 0.353	0.056 ± 0.008	1.323 ± 0.229	1.501 ± 0.292	1.585 ± 0.288	
15.93	4.368 ± 0.412	0.045 ± 0.009	0.882 ± 0.252	1.013 ± 0.327	1.632 ± 0.325	
22.90	3.755 ± 0.505	0.023 ± 0.012	0.739 ± 0.319	0.586 ± 0.395	2.175 ± 0.409	
ESO-LV 4880490 - MJ						
−22.12	4.001 ± 0.332	0.020 ± 0.011	0.977 ± 0.345	0.850 ± 0.340	0.419 ± 0.377	
−16.05	3.550 ± 0.257	0.031 ± 0.008	0.755 ± 0.251	1.023 ± 0.243	0.867 ± 0.269	
−11.27	3.496 ± 0.224	0.046 ± 0.007	0.960 ± 0.232	0.980 ± 0.227	0.981 ± 0.239	
−7.95	3.730 ± 0.188	0.039 ± 0.006	1.010 ± 0.199	1.210 ± 0.198	1.062 ± 0.206	
−5.59	3.704 ± 0.163	0.047 ± 0.005	1.204 ± 0.173	1.589 ± 0.177	1.498 ± 0.186	
−3.86	3.530 ± 0.170	0.046 ± 0.005	0.992 ± 0.172	1.240 ± 0.187	1.252 ± 0.188	
−2.49	3.539 ± 0.160	0.046 ± 0.005	0.887 ± 0.164	1.402 ± 0.182	1.059 ± 0.183	
−1.25	4.004 ± 0.143	0.049 ± 0.004	1.297 ± 0.143	0.950 ± 0.159	1.237 ± 0.158	
−0.01	3.840 ± 0.151	0.064 ± 0.005	1.143 ± 0.157	1.252 ± 0.179	1.170 ± 0.170	
1.24	3.685 ± 0.148	0.040 ± 0.005	0.963 ± 0.155	1.262 ± 0.174	0.727 ± 0.166	
2.47	3.923 ± 0.167	0.037 ± 0.005	0.832 ± 0.169	1.116 ± 0.190	1.154 ± 0.178	
3.85	3.380 ± 0.187	0.043 ± 0.005	0.717 ± 0.180	1.015 ± 0.202	0.981 ± 0.186	
5.46	3.499 ± 0.205	0.044 ± 0.006	0.774 ± 0.194	1.156 ± 0.219	1.037 ± 0.199	
7.56	3.624 ± 0.198	0.047 ± 0.006	1.111 ± 0.192	1.065 ± 0.217	0.534 ± 0.198	
10.53	3.835 ± 0.218	0.052 ± 0.006	1.172 ± 0.211	1.416 ± 0.239	1.248 ± 0.219	
14.72	3.636 ± 0.303	0.022 ± 0.007	0.781 ± 0.241	1.206 ± 0.281	0.889 ± 0.253	
21.96	3.657 ± 0.496	0.040 ± 0.010	1.175 ± 0.305	0.511 ± 0.382	0.796 ± 0.330	
ESO-LV 4880490 - MN						
−2.40	3.124 ± 0.314	0.036 ± 0.008	0.998 ± 0.251	1.352 ± 0.365	1.342 ± 0.358	
−1.35	3.003 ± 0.290	0.028 ± 0.007	0.754 ± 0.214	0.369 ± 0.335	1.579 ± 0.317	
−0.73	4.031 ± 0.276	0.047 ± 0.006	0.979 ± 0.196	1.249 ± 0.310	0.923 ± 0.295	
−0.23	3.636 ± 0.274	0.045 ± 0.006	0.871 ± 0.203	1.563 ± 0.303	1.001 ± 0.294	
0.26	3.631 ± 0.323	0.058 ± 0.007	1.133 ± 0.245	0.597 ± 0.350	1.108 ± 0.337	
0.88	3.518 ± 0.341	0.061 ± 0.007	1.679 ± 0.251	1.093 ± 0.357	1.053 ± 0.324	
1.74	3.140 ± 0.393	0.068 ± 0.008	1.242 ± 0.286	1.435 ± 0.398	0.287 ± 0.382	
3.36	3.069 ± 0.466	0.051 ± 0.010	1.077 ± 0.339	0.983 ± 0.463	0.583 ± 0.443	
ESO-LV 5340200 - MJ						
−13.73	4.142 ± 0.412	0.117 ± 0.013	2.845 ± 0.370	1.768 ± 0.466	0.346 ± 0.395	
−5.70	3.540 ± 0.201	0.129 ± 0.006	2.539 ± 0.173	1.871 ± 0.216	1.330 ± 0.178	
−3.96	3.641 ± 0.151	0.130 ± 0.005	2.371 ± 0.133	2.060 ± 0.165	1.406 ± 0.136	
−2.99	3.361 ± 0.145	0.143 ± 0.004	2.896 ± 0.124	2.175 ± 0.148	1.585 ± 0.131	
−2.38	2.989 ± 0.147	0.131 ± 0.005	2.315 ± 0.126	1.961 ± 0.156	1.572 ± 0.132	
−1.87	3.209 ± 0.121	0.135 ± 0.004	2.710 ± 0.106	2.198 ± 0.130	1.865 ± 0.114	

Table A2 – continued

(1)	(2)	(3)	(4)	(5)	(6)
-1.37	2.890 ± 0.118	0.146 ± 0.004	2.902 ± 0.109	2.297 ± 0.137	1.714 ± 0.122
-1.01	2.985 ± 0.115	0.148 ± 0.004	2.493 ± 0.106	2.286 ± 0.134	1.844 ± 0.124
-0.76	2.950 ± 0.122	0.155 ± 0.004	2.652 ± 0.113	2.392 ± 0.142	2.018 ± 0.133
-0.51	2.942 ± 0.104	0.159 ± 0.004	3.009 ± 0.099	2.415 ± 0.126	2.024 ± 0.117
-0.26	2.746 ± 0.085	0.178 ± 0.003	3.327 ± 0.083	2.523 ± 0.106	2.126 ± 0.099
-0.01	2.980 ± 0.074	0.178 ± 0.003	3.162 ± 0.073	2.637 ± 0.094	2.103 ± 0.090
0.24	2.932 ± 0.071	0.183 ± 0.003	2.983 ± 0.070	2.581 ± 0.090	2.084 ± 0.086
0.49	2.828 ± 0.082	0.195 ± 0.003	2.900 ± 0.078	2.713 ± 0.104	2.339 ± 0.101
0.74	2.893 ± 0.084	0.191 ± 0.003	3.254 ± 0.081	2.646 ± 0.104	1.966 ± 0.103
0.99	2.951 ± 0.099	0.185 ± 0.003	2.953 ± 0.092	2.618 ± 0.117	2.088 ± 0.120
1.24	2.916 ± 0.118	0.181 ± 0.004	2.963 ± 0.109	2.549 ± 0.140	1.661 ± 0.142
1.49	3.158 ± 0.117	0.169 ± 0.004	2.646 ± 0.107	2.443 ± 0.136	1.791 ± 0.141
1.86	3.066 ± 0.104	0.173 ± 0.004	2.847 ± 0.096	2.420 ± 0.122	1.837 ± 0.128
2.36	2.968 ± 0.118	0.151 ± 0.004	2.613 ± 0.112	2.309 ± 0.140	1.845 ± 0.153
2.97	3.526 ± 0.128	0.158 ± 0.004	2.613 ± 0.122	2.295 ± 0.151	1.410 ± 0.167
3.94	3.336 ± 0.125	0.150 ± 0.004	2.733 ± 0.120	2.164 ± 0.156	2.054 ± 0.166
5.61	3.614 ± 0.170	0.138 ± 0.005	2.388 ± 0.163	1.962 ± 0.212	1.432 ± 0.228
12.55	4.065 ± 0.294	0.117 ± 0.009	2.172 ± 0.279	1.711 ± 0.380	0.322 ± 0.407
ESO-LV 5340200 - MN					
-2.24	2.951 ± 0.210	0.161 ± 0.007	2.777 ± 0.219	2.272 ± 0.244	2.353 ± 0.229
-1.54	2.888 ± 0.196	0.155 ± 0.007	2.967 ± 0.201	2.343 ± 0.227	1.907 ± 0.214
-1.18	2.947 ± 0.201	0.175 ± 0.007	2.942 ± 0.211	2.503 ± 0.236	1.650 ± 0.220
-0.93	2.964 ± 0.194	0.169 ± 0.006	3.364 ± 0.189	2.568 ± 0.217	2.191 ± 0.214
-0.68	3.069 ± 0.161	0.166 ± 0.005	3.211 ± 0.153	2.556 ± 0.176	2.132 ± 0.171
-0.43	2.819 ± 0.142	0.177 ± 0.004	3.222 ± 0.125	2.639 ± 0.147	1.773 ± 0.143
-0.18	2.642 ± 0.132	0.181 ± 0.004	3.123 ± 0.115	2.696 ± 0.132	2.712 ± 0.130
0.07	2.686 ± 0.132	0.182 ± 0.004	3.230 ± 0.108	2.651 ± 0.122	2.130 ± 0.122
0.32	3.091 ± 0.141	0.192 ± 0.004	3.299 ± 0.117	2.736 ± 0.132	2.312 ± 0.132
0.57	3.142 ± 0.162	0.193 ± 0.005	3.226 ± 0.136	2.782 ± 0.148	2.845 ± 0.144
0.82	2.860 ± 0.181	0.180 ± 0.005	3.210 ± 0.152	2.707 ± 0.166	2.260 ± 0.164
1.07	2.696 ± 0.202	0.190 ± 0.006	3.177 ± 0.167	2.537 ± 0.182	2.358 ± 0.178
1.43	3.200 ± 0.196	0.168 ± 0.006	2.760 ± 0.164	2.509 ± 0.181	1.889 ± 0.178
2.03	3.596 ± 0.263	0.150 ± 0.008	2.629 ± 0.219	2.212 ± 0.238	1.308 ± 0.226
PGC 26148 - MJ					
-7.43	4.637 ± 0.130	0.132 ± 0.004	2.213 ± 0.162	2.314 ± 0.184	1.284 ± 0.195
-4.70	2.930 ± 0.128	0.179 ± 0.004	2.964 ± 0.169	3.016 ± 0.181	2.272 ± 0.190
-2.40	2.423 ± 0.128	0.194 ± 0.004	3.111 ± 0.162	2.835 ± 0.172	2.437 ± 0.182
-1.19	2.804 ± 0.103	0.153 ± 0.003	3.153 ± 0.122	2.331 ± 0.133	2.124 ± 0.142
-0.75	2.439 ± 0.107	0.128 ± 0.003	2.167 ± 0.122	2.302 ± 0.136	2.098 ± 0.144
-0.50	2.767 ± 0.095	0.136 ± 0.003	2.009 ± 0.112	2.385 ± 0.124	2.255 ± 0.130
-0.25	2.594 ± 0.098	0.148 ± 0.003	2.562 ± 0.115	2.623 ± 0.132	2.320 ± 0.133
0.25	2.652 ± 0.107	0.150 ± 0.003	2.912 ± 0.128	2.457 ± 0.147	2.213 ± 0.150
0.50	3.386 ± 0.111	0.141 ± 0.003	2.817 ± 0.132	2.239 ± 0.147	2.195 ± 0.152
0.85	3.319 ± 0.108	0.157 ± 0.003	2.972 ± 0.132	2.555 ± 0.147	1.943 ± 0.151
1.65	2.793 ± 0.124	0.190 ± 0.004	3.200 ± 0.157	3.347 ± 0.172	2.987 ± 0.176
3.63	2.696 ± 0.136	0.185 ± 0.004	2.755 ± 0.175	2.941 ± 0.192	2.257 ± 0.194
6.69	4.193 ± 0.139	0.110 ± 0.004	2.052 ± 0.172	2.768 ± 0.189	1.751 ± 0.191
PGC 37759 - MJ					
-11.13	4.090 ± 0.232	0.009 ± 0.007	2.071 ± 0.285	1.356 ± 0.360	1.353 ± 0.340
-7.89	3.859 ± 0.239	0.002 ± 0.007	2.058 ± 0.269	2.089 ± 0.345	1.457 ± 0.325
-6.13	4.461 ± 0.212	0.010 ± 0.006	2.196 ± 0.252	1.255 ± 0.319	1.519 ± 0.304
-4.62	3.852 ± 0.212	0.035 ± 0.007	2.175 ± 0.264	1.982 ± 0.332	1.842 ± 0.313
-3.23	2.892 ± 0.203	0.056 ± 0.006	2.951 ± 0.246	1.834 ± 0.310	1.880 ± 0.291
-2.13	2.964 ± 0.203	0.062 ± 0.006	3.152 ± 0.240	2.244 ± 0.307	1.969 ± 0.290

Table A2 – *continued*

(1)	(2)	(3)	(4)	(5)	(6)
-1.22	2.693 ± 0.194	0.059 ± 0.006	3.535 ± 0.214	2.738 ± 0.281	2.049 ± 0.261
-0.61	3.087 ± 0.161	0.049 ± 0.005	3.003 ± 0.174	2.698 ± 0.228	1.987 ± 0.214
-0.25	3.097 ± 0.185	0.036 ± 0.006	3.021 ± 0.193	3.052 ± 0.256	2.061 ± 0.243
0.00	2.267 ± 0.175	0.055 ± 0.005	2.932 ± 0.182	2.625 ± 0.241	2.149 ± 0.231
0.25	2.997 ± 0.163	0.054 ± 0.005	2.862 ± 0.169	2.402 ± 0.221	2.186 ± 0.221
0.50	3.225 ± 0.180	0.062 ± 0.006	3.072 ± 0.186	2.506 ± 0.244	2.229 ± 0.248
0.86	2.859 ± 0.165	0.039 ± 0.005	2.734 ± 0.169	1.789 ± 0.225	2.153 ± 0.232
1.47	2.985 ± 0.187	0.069 ± 0.006	3.292 ± 0.190	3.108 ± 0.263	2.075 ± 0.262
2.37	2.827 ± 0.213	0.064 ± 0.007	3.233 ± 0.208	2.760 ± 0.293	2.078 ± 0.302
3.37	3.356 ± 0.202	0.030 ± 0.006	2.259 ± 0.196	1.956 ± 0.279	2.002 ± 0.293
4.57	3.470 ± 0.208	0.041 ± 0.007	2.912 ± 0.206	2.727 ± 0.299	1.843 ± 0.318
6.41	3.498 ± 0.208	0.005 ± 0.006	2.498 ± 0.200	1.870 ± 0.298	1.651 ± 0.316
8.07	4.539 ± 0.217	-0.006 ± 0.007	1.888 ± 0.210	2.420 ± 0.321	1.451 ± 0.343
10.30	4.234 ± 0.227	0.006 ± 0.007	2.631 ± 0.226	2.292 ± 0.344	1.396 ± 0.370
PGC 37759 - MN					
-12.36	3.411 ± 0.970	0.157 ± 0.035	-0.377 ± 1.085	1.802 ± 1.259	1.793 ± 1.093
-2.11	3.306 ± 0.248	0.165 ± 0.010	2.983 ± 0.297	1.560 ± 0.341	2.117 ± 0.289
-0.54	2.286 ± 0.217	0.165 ± 0.009	2.936 ± 0.258	1.862 ± 0.295	2.168 ± 0.251
0.05	2.742 ± 0.191	0.184 ± 0.007	3.417 ± 0.227	3.299 ± 0.254	2.459 ± 0.210
0.53	2.614 ± 0.218	0.178 ± 0.009	3.158 ± 0.266	3.274 ± 0.292	2.455 ± 0.245
1.80	2.685 ± 0.241	0.169 ± 0.010	1.791 ± 0.298	2.448 ± 0.332	2.298 ± 0.283
10.48	4.585 ± 0.820	0.253 ± 0.031	3.777 ± 0.950	-1.004 ± 1.114	1.495 ± 0.994